Doctoral theses at NTNU, 2013:81

Knut Skogstrand Gjerden

Role of quenched disorder in fracture front propagation

Doctoral Thesis

NTNU
Norwegian University of Science and Technology
Thesis for the degree of Philosophiae Doctor
Faculty of Natural Sciences and Technology
Department of Physics

NTNU – Trondheim
Norwegian University of
Science and Technology

Knut Skogstrand Gjerden

Role of quenched disorder in fracture front propagation

Thesis for the degree of Philosophiae Doctor

Trondheim, February 2013

Norwegian University of Science and Technology
Faculty of Natural Sciences and Technology
Department of Physics

NTNU – Trondheim
Norwegian University of
Science and Technology

NTNU
Norwegian University of Science and Technology

Thesis for the degree of Philosophiae Doctor

Faculty of Natural Sciences and Technology
Department of Physics

ISBN 978-82-471-4261-5 (printed version)
ISBN 978-82-471-4262-2 (electronic version)
ISSN 1503-8181

Doctoral theses at NTNU, 2013:81

Printed by Skipnes Kommunikasjon as

To all those with imagination in their hearts
And to those who teach to look things up and investigate.

Abstract

The process of materials fracture is not yet understood across all levels. This thesis contains detailed description on a model of in-plane fracture along with results obtained using this model. The results from the model are in very good agreement with experimental observations, both with respect to the static scaling of the front (morphology) and a dynamic study of the underlying processes. This is quite remarkable, considering our model is quasistatic, meaning that the dynamics are time independent.

Using this model, I have found two scaling regimes which corresponds to the two different regimes found experimentally for in-plane fracture. This is the first model to successfully reproduce these two scaling regimes, allowing us to clearly state the important processes in this constrained form of fracture. Only the geometry is constrained, any material obeying the quite general assumptions in the model should contain the same processes and fracture in the same way.

The results indicate that a percolation process is controlling the fracture on small scales. At larger scales, the elastic material properties leads to a stress concentration which eventually constrains damage formation to the immediate area near the fracture front. In the large scale regime I have measured a roughness exponent of

$$\zeta_{\text{large}} = 0.39 \pm 0.04 \ .$$

In the small scale regime, I show data consistent with and present evidence based on several different analyses for a roughness exponent of

$$\zeta_{\text{small}} = \frac{2}{3} \ .$$

Foreword

This thesis is submitted to the Norwegian University of Science and Technology (NTNU) for partial fulfillment of the requirements for the degree of philosophiae doctor. The work has been performed at the Department of physics, NTNU, Trondheim, with Professor Alex Hansen as supervisor.

The study has been carried out during the period of December 2008 to December 2012, which includes various teaching work performed for NTNU; most notably as teaching responsible for several groups of students during their introductory laboratory courses in physics at NTNU. My teaching duties amount to a workload of approximately 25% during the four-year period. In addition, I have followed a selection of courses amounting to one full semester. These courses are also part of the requirements for the degree of PhD.

My doctoral work has been funded by the Norwegian Research Council (NFR) through grant number 177591/V30. Specific parts of my work, relating to the graphics card acceleration of the code central to the project, were performed as a guest at EPCC, Edinburgh under the HPC-EUROPA2 project (project number: 228398) with the support of the European Commission Capacities Area - Research Infrastructures Initiative.

The code used for this study has been developed by me, with ideas and input from my colleague Arne Stormo and in particular Alex Hansen. Arne and I have worked on essentially the same problem, and have developed separate codebases in mild cooperation and competition, so we can discuss the technical details to great depths. The simulations have been primarily run on my desktop and, with the graphics card enhancements, laptop computers. Parts has also been run of the GPU testbed of HECToR, the UKs national high performance computing service, which is provided by UoE HPCx Ltd at the University of Edinburgh, Cray Inc and NAG Ltd, and funded by the Office of Science and Technology through EPSRCs High End Computing Programme.

In addition to the people I have already mentioned, I must mention some of the friends and colleagues who have to a great extent made up my day-to-day social network during these years: Tor Nordam, Paul Anton Letnes, Christer H. Ersland, Morten Grøva, Zbigniew Rozynek, Santanu Sinha, along with many other "inhabitants" of the different halls in the science building.

I have met many people that deserve mentioning during travels and conferences who in general have made life much more enjoyable. Unfortunately, I cannot list them because they are too many to remember all in the writing moment and I refuse to prioritise among them. However, special mention goes to Elisabeth Bouchaud, for being the second person to threaten my life if I failed my task. Challenge complet!

I must also thank my family and friends outside the physics community for the

questions "so, what do you do, really?" which has made me continuously rethink my thesis and its presentation. I have tried, and it is my sincerest hope that the following pages will answer that question in a manner accessible to all. Albeit a bit longer answer than most of you were hoping for, but hopefully still understandable. Caveat familia et familiarum ateknologia: You'll have to try though, please don't give up straight after the table of contents. And you can skip ahead to chapter 4 after finishing section 3.1. The remainder of the third chapter is very technical at times and is for the most part not required to understand the results.

Penultimately, I want to use this opportunity to share my appreciation of my girlfriend, come fiancee, come wife, Hanna Maja. She is truly beautiful in every respect.

I will remember this time very fondly and am thankful for all opportunities I have gotten. Oh, and I used to hate long forewords, but now I understand how they get so long.

Knut Skogstrand Gjerden

Trondheim, January 2013

Addendum to the foreword of the electronic edition

My cat loves you for not printing this thesis. Well, probably not, but giving him a treat would help.

As a part in making this manuscript more easily understandable, I have included a glossary at the end of the main text. If you come across a word that you would have liked an explanation for, try to click on it and see if you are transported to the glossary section.

Addendum to the foreword of the printed edition

This thesis uses a real-time augmented visualisation tool. At the bottom of most pages, you will find a small image of a fracture front. The following numbers and terms will make sense after you have read the thesis: On odd-numbered pages, small-scale behaviour is shown, and on even-numbered pages, large-scale behaviour is shown. The common simulation parameters are $L = 256$ and $g = 0.00625$. Small-scale behaviour is exemplified at $E = 500.0$ and large-scale at $E = 0.256$. For the first frames, $\langle h \rangle \lessapprox 400$, and for the final frames, $\langle h \rangle \lessapprox 500$. 750 bonds are broken between each frame.

If you did not print this document yourself and still hold a hardcopy in your hands, odds are that you have a first edition official print. Congratulations. The odds would also be in favour that you were actually present at my public thesis defense. I thank you for coming to listen to me.

If you did print this document yourself, please consider stopping printing out documents. The electronic version has more features and is author-recommended.

List of papers

List of papers included in this thesis

Paper I

Knut S Gjerden, Arne Stormo and Alex Hansen

A model for stable interfacial crack growth

Journal of Physics: Conference Series, **402**:012039 (2012) [18]

This is the first description of the model we have developed in print. A method to keep driving a fracture indefinitely is introduced. We present snapshots from simulations, showing very different fracture front behaviour in two different elasticity regimes. Preliminary results showing two different (but lower than the current values) scaling exponents are presented.

Paper II

Arne Stormo, Knut S Gjerden and Alex Hansen

Onset of localization in heterogeneous interfacial failure

Physical Review E **86**, 025101(R) (2012) [57]

This paper studies the breakdown process in our model in globally uniform tension, i.e., no fracture front. We show a change from randomly broken bonds to localised broken bonds through variation of the elastic control parameter. This is not a phase transition, but a crossover from one dominating process to the other.

Paper III

Knut S Gjerden

Making the case of GPUs in courses on computational physics

Submitted to European Journal of Physics [16]

This paper discusses the use of graphic processor units for numerical calculations. It shows how much benefit could be expected for relatively little change in the simulation code. In many cases, this technology represents an untapped potential in most computers.

Paper IV

Knut S Gjerden, Arne Stormo and Alex Hansen

Universality classes in constrained crack growth

Submitted to Physics Review Letters [20]

We present results showing two scaling regimes with roughness exponents $\zeta = 2/3$ and $\zeta = 0.39$. The difference in behaviour is due to the competition between stress concentration and a percolation process. For a stiff material, percolation is the dominating process, while for softer materials, stress concentration is the crucial process. The elasticity is coupled to a length scale, so stiff materials correspond to small scale simulations, and soft materials correspond to a large length scale. A transition in the control parameter is found, similar to the relation between randomness and localisation found in Paper II. We show how easy it is to measure an exponent $\zeta \approx 0.6$ in this system. We also show clear evidence for the percolation process leading to $\zeta = 2/3$ in the form of scaling of the front width evolution and fractal dimension of the front.

Paper V

Knut S Gjerden, Arne Stormo and Alex Hansen

Local dynamics of a randomly pinned crack front: A numerical study

In preparation [19]

Using the waiting time matrix method, we study the dynamics of the fracture front in our quasi-static model. The results are in very good agreement with experimental data also obtained using the same method. We study the local scaling properties of the front behaviour and indicate a dependence on the roughness exponents 2/3 and 0.39.

Paper VI

Knut S Gjerden and Arne Stormo

On the universality classes and scaling exponents found in interfacial brittle fracture

In preparation [17]

Summing up the different scaling relations, we analyse data from both experimental and numerical sources on scaling in in-plane fractures, and derive new relations. As a result, both experimental data and simulations fit with the scaling exponents of the front, 2/3 on small scales and 0.39 on large scales.

My contribution to the papers

Paper I

I wrote the simulation code and ran the simulations for this paper. This also applies to papers III-VI. This paper was published in volume 402 of Journal of Physics: Conference Series, along with other proceedings of the Conference on Computational Physics (CCP2011) held in Gatlinburg, Tennesee. The papers were peer reviewed. I am responsible for all the data and and illustrations to this paper, and I wrote most of the text. Some of the figures and text were modified during the preparation of the manuscript in collaboration with the co-authors. All authors were heavily involved in the development of the model.

Paper II

Arne Stormo and I have been developing the model we use in parallel, using different programming languages. The combination of cooperation and competition means that we can discuss the model and results in great detail. Thus I could provide numerical validation of the results presented in the paper. I also contributed to discussions and the analytical derivations in the paper.

Paper III

As the only author, I am solely responsible for this paper (text, data and figures).

Paper IV and V

I am responsible for all the data and made all the figures in these papers. I wrote up the initial texts of the papers, which was then modified with help from my co-authors, mostly Alex Hansen. All authors have participated in discussion and preparation of the manuscripts.

Paper VI

This paper uses data from other sources. I collected this data and supplemented with data of my own. I wrote most of the text. More data will be collected with the assistance of Arne Stormo. This paper requires more work, but is included in this thesis for completeness.

Contents

Chapter 1

Introduction

> *Begin at the beginning," the King said, gravely, "and go on till you come to an end; then stop.*
>
> Lewis Carroll, *Alice in Wonderland*, 1899

In this chapter, I will introduce the most central concepts of fracture study relevant to this thesis. The purpose is to provide a minimum platform for all readers and give some intuition so that the results will be more accessible for non-experts. Next chapter will present the evolution this specific branch of statistical fracture study and will serve to further motivate the work behind this thesis.

In chapter 3, the model central to my work is presented in detail. This is the most technical chapter of this thesis. The results are presented over two chapters, and are primarily centered on the morphology of the fracture front. Chapter 4 discusses the shape of the fracture front, while chapter 5 addresses the dynamic processes which create the front. The final chapter sums up my results and contributions to this field of study.

1.1 Lightspeed introduction to fracture mechanics from a physicist's view

The Griffith criterion is to fracture mechanics as the Hippocratic oath is to medicine. It is often incorrectly considered the foundation of the field. As high-priest Imhotep treated injuries and diseases about two thousand years before Hippocrates practiced medicine [55], so did Leonardo da Vinci perform fracture tests on iron wires [3] three hundred years before the person who usually gets most of the credit was born. Since da Vinci's investigations were only qualitative, much of the honour passes to the

Briton engineer Griffith due to his quantitative work and formulation of a fracture criterion [22].

During the 1950s, the American Irwin modified the work of Griffith to develop the *energy release rate* concept and later, he used the work of Westergaard [61] to come up with the *stress-intensity factor*, K [30]. These are both examples of single-parameter descriptions of fracture in linear elastic fracture mechanics (LEFM). In LEFM, the central ideas are that material breaks without any permanent deformation (ideal brittle fracture)[1] and that up to the breaking point, any applied load causes a strain, ϵ, in the material which is *linear* with the *elastic* stress, σ in the material,

$$\sigma = E\epsilon. \tag{1.1}$$

E is the Young's modulus, a material property.

An illustration of the three ideal fracture modes in fracture mechanics is found in Figure 1.1. For many standard geometries, the respective stress-intensity factors can be exactly calculated, and the results are superimposed to give the total stress-intensity factor $K_{\text{tot}} = K_I + K_{II} + K_{III}$. In materials testing, all modes are used, while in physics research, predominantly mode I is used. This is in part because physicists are very interested in the fracture surface left behind in the process. In modes II and III, there is a high likelihood that the surface is worn down as part of the loading process. However, all real life fracture situations are at some point a mix of all three modes.

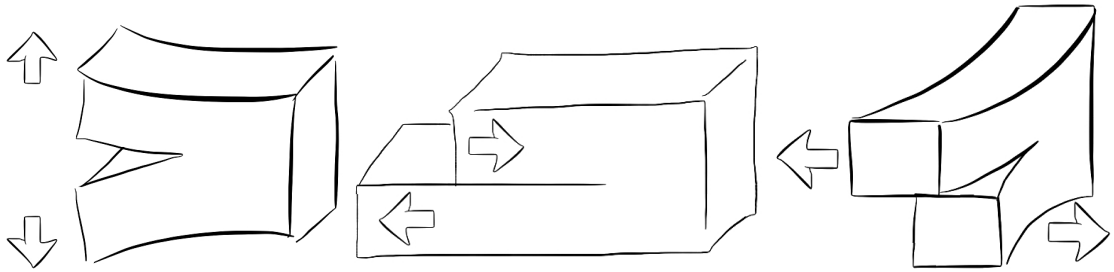

Figure 1.1: The three modes of fracture: I, opening or tension; II, sliding or in-plane shear; and III, tearing, or out-of-plane shear.

LEFM is an idealised approximation. For high enough stresses, the linearity of (1.1) is broken due to plastic deformation effects in the material under stress. In the mid-1960s, Rice of Brown University modeled plastic effects as non-linear elastic behaviour in his J-integral formulism [46]. This was the first major contribution to non-linear elastic fracture mechanics (NLEFM). Through the J-integral, more of the bulk material could be modeled. The fracture models were more correct, and the understanding of the fracture process penetrated deeper into the material, closer to the crack tip where the stresses are highest.[2]

[1] Loading is a reversible process in LEFM up to the critical point where fracture occurs.

[2] The stress is actually highest a little bit ahead of the crack front [3].

The study of both LEFM and NLEFM continued with several more contributors. Including plastic deformations led to elasto-plastic fracture mechanics (EPFM), which is by many considered a generalisation of NLEFM. The technical difference between the three is that when loading and unloading a sample in LEFM, the stress-strain curve is a straight line for loading and the same straight line for unloading (following the same straight line "backwards"). In NLEFM, this curve does not need to be a straight line anymore, but the paths for loading and unloading are still the same. In EPFM, the loading curve does not need to be straight, but the unloading curve is the same straight line as for unloading in LEFM. This results in a permanent shift on the strain-axis for the sample, indicating irreversible damage in the sample (something has "been stretched too far").

Current fracture mechanics models are not simple one-parameter descriptions. One can very accurately predict bulk behaviour for most of the material using more complex two- or three-parameter descriptions [3]. That is most of the material, but not all.

The bottom line is, after all the development in fracture mechanics study, there is still a region very close to the fracture tip or front which is not completely understood. This region of very high stresses is called the fracture process zone (FPZ). The two main approaches to study the FPZ are coined bottom-up and top-down. Molecular dynamics (MD) is an example of a bottom-up approach, where the material or sample in question is directly modeled by individual atoms or molecules. The interactions of the molecules are set and some initial conditions are given and then the system is followed in time as it evolves. This approach is currently quite limited in resolution in time and space because it is very computationally intensive as only a small sample contains a very large number of molecules. The typical time scale in current MD tools is in nanoseconds. It is my opinion that this approach shows significant promise, but is not yet fully mature for use in materials testing and engineering. However, MD is starting to be used as a tool to study fracture from a physicist's point of view [44].

A top-down approach usually entails an analytical starting point in the form of continuum equations derived from established physical relations, which is then applied to a new problem.[3] This has been the typical approach which has lead to the current situation.[4] One starts with large scale behaviour and tries to work backwards to make statements on the underlying processes on a smaller scale.

[3]Example: An iron die is considered a cubic shape with specific surface and bulk properties dependent on the physical size and material of the die. The bottom-up way of seeing the same die would be as a collection of iron atoms in a specific crystal structure. Established vs. emergent properties.

[4]As well as several jokes regarding spherical cows in a vacuum.

Statistical physics and brittle interstitial fracture

In the field of statistical physics, the central concept is to construct a model with the minimal amount of assumptions and elements. One then creates an ensemble of many systems where each system obeys the rules of the model but they are all individually different based on some random element. Based on this ensemble of systems, statistics is used to draw conclusions on common properties which typically emerges due to complex collective behaviour of the elements in each system. Specifically, for this thesis, I have simulated a very large number of fracture fronts under different conditions. The results of statistical analyses on these fronts and conclusions based on these results are presented herein.

Glass shattering, a twig breaking neatly in half with a loud snap, a dinner plate crashing to the floor: These are examples of brittle fracture. Brittle fracture is typically associated with LEFM. Fracture events can be divided into brittle and ductile. Ductile fracture is fracture due to plastic deformation effects. Rubber and other plastics are examples of materials typically undergoing ductile fracture. The fracture type is not dependent on the material per se, but other properties such as temperature, loading speed and dislocation density, to name some. The phenomenon is known as ductile-brittle transition and temperature is the primary control parameter.

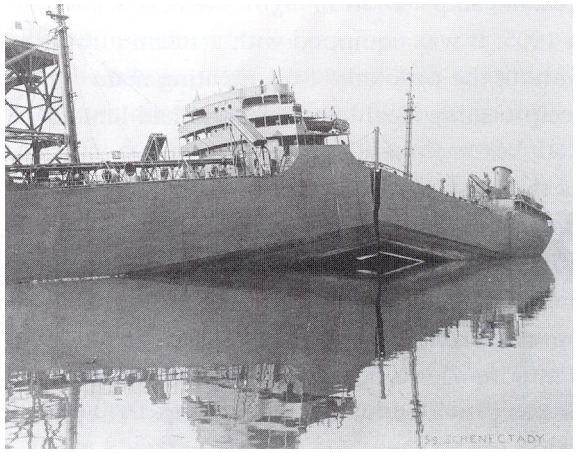

Figure 1.2: The SS Schenectady after massive structural failure in January 1943 at Swan Island, Portland, Oregon.

Cooling down rubber will make it lose its ductility and undergo brittle fracture. Even a banana, when sufficiently chilled, will undergo brittle fracture. Figure 1.2 shows a photography taken of the tanker SS Schenectady which broke almost in half on January 16 1943, only 24 hours old [60]. Only the bottom plate held the ship together. The ship was reported to break suddenly and very audibly, which tends to indicate brittle fracture [60]. Initial reports on the event were inconclusive, there was no obvious reason for why the ship should have failed. At a later time, the leading theory would be that cold weather embrittled the low-grade steel plates used, which,

coupled with reports on poor welding [60] can explain the massive structural failure.

Since all materials can undergo brittle fracture and it is a less complex fracture mechanism than ductile fracture, this is the starting point for many physical models of fracture; including the model presented in this thesis.

Fracture is unarguably a complex process. To reduce the complexity, one can study fracture in lower than three dimensions. The one-dimensional fracture geometry could represent fracture in paper, while an example illustrating two-dimensional fracture would be the peeling of an adhesive off of a substrate. The different geometries are illustrated in Figure 1.3. The next chapter will present an experimental setup of the 2D geometry, which is technically a 3D fracture constrained to two dimensions. This setup is called *interstitial* or *in-plane* fracture because the fracture front is constrained to move in one plane only. My work is based on in-plane fracture under the assumption that this does not change the physics of the situation, but it offers a great reduction of the complexity.

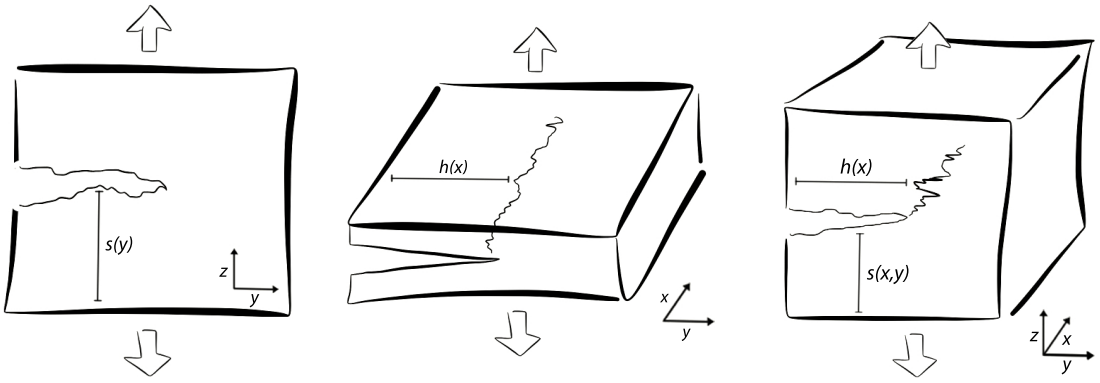

Figure 1.3: Illustration of 1D, 2D and 3D fracture geometry. The function $s(y)$ characterises the fracture surface and the function $h(x)$ gives the height of the interface between broken and unbroken material as measured from the edge of the material. In other words, $h(x)$ denotes how far into the sample the fracture has traversed. The 2D geometry is a three-dimensional system where the fracture is constrained to move in one plane only. This is also called in-plane fracture and is the specific geometry I have been working with.

1.2 Fractals, self-affinity and universality

The term fractal can carry many meanings and is not straightforward to clearly define. Properties that the mathematical construct that is a fractal should have are infinite *self-similarity*, iterativeness, and have a *fractal dimension*. Most important of these in this setting is the self-similarity and the fractal dimension. A typical example of a fractal curve is the Koch curve, its construction depicted in Figure 1.4.

This curve is nowhere differentiable, another property shared among fractals, and so cannot be treated by traditional mathematics.

The concept of self-similarity can be thought of through magnification. A shape is self-similar if, by magnifying it with a factor f, it is indistinguishable from its unmagnified self. In the case of the Koch curve, $f = 3$. This can be seen in Figure 1.4: The entire shape at $i = x$ scaled down to a third is equal to the first and last thirds of $i = x + 1$, and also the top third if $1 < x \leq \infty$.

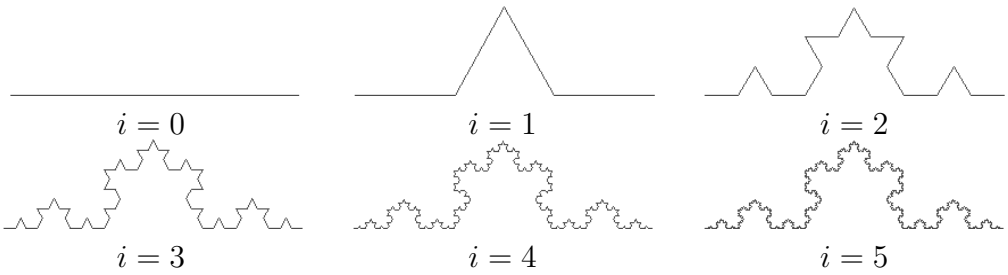

Figure 1.4: The first iterations of the Koch curve. The curve is constructed by turning the middle third of any line into an equilateral triangle. Already at $i = 5$, the detail is lost at this level. Note the *self-similarity* in the figures. The first third of the next iteration is identical to the entire current iteration scaled down to a third.

A point has zero dimensions, a line has one dimension, and you may have thought that any shape you can draw on a flat piece of paper has two dimensions. This is not completely true, as certain objects have non-integer dimensionality. The simplest way of thinking of fractal dimensions may be with respect to measuring lengths (or circumferences). Using Figure 1.4 and starting from $i = 0$, using a measuring stick as long as the line, the result is 1 when you measure the length of the line. If you now break the measuring stick into three identical pieces and only use one of them, the result is 3. If you now measure for $i = 1$, the result is not 3, but 4. For every time you break the measuring stick into three pieces, the measured result increases by a factor four. The fractal dimension of the Koch curve is

$$D_f = \frac{\log(4)}{\log(3)} \approx 1.2619. \tag{1.2}$$

Not just mathematical constructs have a fractal dimension. Richardson measured the length of the coastline of Britain as having a fractal dimension of 1.25, reported by Mandelbrot [41]. A few years later, the coastline of Norway was reported to have a fractal dimension of 1.52 [15]. Several objects in nature have *approximate* fractal properties, such as frost crystals, lightening bolts, cauliflower, and Romanesco broccoli. None of these objects are fractals, as none of them are infinitely self-similar.

Self-affinity and universality

Self-affinity is closely related to self-similarity. If self-similarity can be considered isotropic magnification, then self-affinity is anisotropic magnification (different magnification in the x- and y-directions). For the next chapter, it is important to separate the terms object/curve and function with respect to this isotropy or anisotropy. "Object" is the general term and can refer to any shape in any dimension. "Curve" is specifically used to describe a part or projection of an object which can be drawn in a two-dimensional coordinate system with a starting point and an end point a distance apart. A "function" is any curve that can be described by a general expression $f(x)$ such that there is a one-to-one relation $f(x) = y$. Objects and curves can be fractal and thus exhibit self-similarity and have a fractal dimension. Functions are generally *not* fractals and can typically be self-affine, not self-similar. Objects and curves can also be self-affine, and the term self-affine fractal is sometimes used, though I am not sure if this a technically valid description, so I will not be using this term. The usage of this term is probably connected to the fact that on small length scales, self-affine functions can have a fractal dimension different from the trivial $D_f = 1$ which they have on large length scales [4, 27].

A self-affine function follows a scaling relation

$$f(x) \sim \lambda^{-\zeta} f(\lambda x) \,, \tag{1.3}$$

where ζ is often labeled H and called the Hurst or Hölder exponent [4]. These exponents are defined more stringently than the uses we will have for this exponent, so for now I use ζ and call it the self-affine exponent.

Universality refers to the collection of self-affine functions into groups called *universality classes* with similar values for the self-affine exponent. With these terms explained, we dive directly into chapter 2.

Chapter 2

Historical and mathematical context

> *In girum imus nocte et consumimur igni.*
>
> Unknown, -, -

Is it possible to (quantitavely) describe fractures in a simple, yet accurate manner? This story begins in 1984, when Mandelbrot et al. [42] suggested that fractures were fractals and the morphology of fractures could be described in the language of fractal dimensions. With the current definitions, fractures are not infinitely self-similar and thus *not* fractals. In 1990, Bouchaud et al. [9] proposed that fractures were self-affine, and that the self-affine scaling properties were universal, i.e., not dependent on the fracturing material. This was to be the beginning of a long discussion on the values of the self-affine exponents and their division into universality classes.

A few years later, Bouchaud et al. [10] suggested that a fracture surface could be regarded as the result of a fluctuating elastic line passing through the material. Schmittbuhl et al. [54] proposed that one could simplify the situation by constraining the crack growth to a weak plane between two elastic solids. This system would be experimentally realised in 1997 by Schmittbuhl and Måløy [53]. The experimental setup consisted of two Plexiglas (PMMA) plates, first sandblasted with glass beads of different size distributions to create a local variation of the surface, and then sintered together to form a single block of PMMA. This specific material is transparent under visible light, but when the block is put under load and pulled apart, a crack front develops in the weak plane and the material is separated into two fracture surfaces. When the material separates, the block as seen from above or below turns opaque. This is the situation illustrated in Figure 1.3 as the 2D geometry. The experimental setup allows for direct visualization of the fracture front during the fracturing process [53].

Schmittbuhl et al. [54] presented a model on interstitial (in-plane) fracture growth based on the idea of the fluctuating line. This model, along with close derivatives of it, will be referred to as the *fluctuating line model*. The main result of Schmittbuhl et al. was to determine a value for the self-affine exponent. A slight extension of (1.3),

$$p(\lambda^{\zeta} h, \lambda x) = \lambda^{\zeta} p(h, x) \ , \tag{2.1}$$

applies when $p(h, x)$ is the probability density that the crack is at height h at x when it is $h = 0$ at $x = 0$ and $h = h(x)$ according to Figure 1.3. In the context of fracture, the self-affine exponent ζ is called the *roughness exponent*.

At this point it is extremely important to get the definitions correct. There are more than one roughness exponent. From Figure 1.3, note that the fracture in general traverses the xy-plane from one end of the material to the other, irrespective of geometry. Thus, the fracture front sets a directionality. *As* the front moves through the material, $y(t) = h(x, t)$ gives all the information about the fracture front, *if this is accessible*. Immediately *after* the front has passed, a surface $z = s(x, y)$ is left behind (two surfaces really, but I'm only referring to the lower one). The surface $s(x, y)$ can be extracted *after* a sample has fractured, the movement $h(x)$ (implicitly $h(x, t)$) has to be recorded *during* the fracture process. From $h(x)$, a scaling exponent in the x-direction can be extracted through (2.1). This is the *in-plane* roughness exponent. Similarly, from $s(x, y)$, two exponents can be extracted. The *out-of-plane* roughness exponent exponent also in the x-direction, and the *along-plane* roughness exponent in the y-direction. The notation for these roughness exponents can vary, so it is important to check which one(s) are being discussed.

Technically, $y(t) = h(x, z, t)$, so there is also an out-of-plane roughness exponent as the fracture front moves. If the two fracture surfaces are perfectly separated after fracture (without suffering additional damage in the process), the two out-of-plane exponents measured should be identical. The idea of constraining the fracture to move in one plane is that the in-plane and out-of-plane exponents are independent of each other so that one does not change when the other is suppressed. This thesis will only discuss the physics of in-plane fracture, not the study of postmortem fracture surfaces. From here on, all references to ζ and the roughness exponent should be taken to mean in-plane.

Back to the story: The first measurements of the roughness exponent in the fluctuating line model reported $\zeta = 0.35$ [54]. However, this did not match the value measured experimentally, $\zeta = 0.55 \pm 0.05$ [53]. This value was later refined to $\zeta = 0.63 \pm 0.03$ through a comparison of several statistical analysis methods [13]. The value from the fluctuating line model was also refined, by Rosso et al. [47], to $\zeta = 0.388 \pm 0.002$. This is still the value with highest accuracy, so $\zeta_{\text{line}} = 0.388$. The discrepancy between simulations and experiments was a big concern.

A short time later, a percolation-type model was proposed by Schmittbuhl et al.

[52][1], which focused on the front moving forward by formation, growth and coalescence of voids ahead of the front. This model predicted a roughness of $\zeta_{\text{coal}} = 0.60 \pm 0.05$ [52], in close agreement with the experimentally obtained value [13, 53].

Schmittbuhl et al. claimed that their model represented a new type of percolation, stress-weighted percolation, with critical exponents different from ordinary percolation (in a gradient). These results were heavily criticised by Alava et al. [1, 2], claiming that gradient percolation (including the model of Schmittbuhl et al. in the use of that term) gives self-similar fronts, not self-affine fronts. This would imply that the measured exponent was not a roughness exponent, because fracture fronts are not self-similar. Shortly thereafter, Hansen et al. [25] showed that the front obtained in gradient percolation is indeed self-affine[2]. This thesis will hopefully provide the final piece to this picture, showing that the ideas proposed in the model of Batrouni, Schmittbuhl and Hansen [5, 52] leads to a self-affine fracture front characterised by the critical exponents of ordinary gradient percolation, not a new percolation class [20].

A few years ago, Santucci et al. [48] analysed larger experimental systems than had been considered earlier in [13, 53]. They reported a crossover between two scaling behaviours; $\zeta_- = 0.60 \pm 0.05$ for small length scales and $\zeta_+ = 0.35 \pm 0.05$ for larger length scales [48]. This was the first time two different exponents were found in the same experiment. The measured exponents were consistent with the damage coalescence model of Schmittbuhl et al. [53] and the fluctuating line model [47, 54], respectively. This led to the idea that there could be two different fracture mechanisms at work on different length scales.

From the fluctuating line perspective, there has been some reports of two different scaling exponents. Ponson et al. [45] showed that their model contained two exponents, one which could be calculated to $\zeta = 1/2$ [59], and one which has to be approximated by other methods ($\zeta \approx 0.39$ [47]) [45]. Ponson et al. suggested that their self-affine front with $\zeta = 0.5$ was consistent with the measured $\zeta \approx 0.57$ (this value was cited as private communication from Santucci et al. dated the year before their results were published [48]) which showed *multi-affinity* [45]. Around the same time, Laurson et al. [36] presented results also showing two different behaviours at different scales: $\zeta = 0.55 \pm 0.05$ and $\zeta = 0.39 \pm 0.03$. The former exponent was argued to be connected to the Larkin length[3], which should give $\zeta = 1/2$ [36]. From the results of Ponson et al., the Larkin argument seems not to be necessary, which was also noted by Tanguy et al.: "At this stage, the Larkin criterion thus seems to be artificially constructed and may call for more thorough study." [59]. This also agrees with Santucci et al. who commented that their crossover length scale between

[1] Based on a model of Batrouni et al. [5] published just before, which did not address in-plane fracture.

[2] The ordinary front was shown to have fractal properties, while the SOS-front was shown to be self-affine.

[3] The Larkin length [35] effectively gives the length scale where elastic force from the fluctuating line balance the pinning force from strong bonds in the material (on average).

ζ_- and ζ_+ was different from the Larkin length scale [48].

This thesis will present work done with a model heavily inspired by the work of Batrouni, Schmittbuhl and Hansen [5, 52]. The model is explained in detail in the following chapter. The model used will be shown to reproduce two scaling regimes with exponents consistent with the experimentally obtained ζ_- and ζ_+ [20]. According to Ponson et al., the fluctuating line model contains the two regimes $\zeta = 1/2$ and $\zeta = 0.39$, and multi-affinity caused the deviation between the small scale results of experiment and model [45]. Our model suggests that simple gradient percolation is behind the small scale behaviour [20]. This will be clarified in this thesis. If our conclusions are correct, the front in the small scale regime should be given by $\zeta = 2/3$ and be self-affine, according to gradient percolation, not multi-affine [25], making our model [18] the first shown to simultaneously contain both scaling regimes seen experimentally for in-plane fracture. By simultaneously I mean that there are models on the creeping motion of an elastic line moving through a disordered material which reproduce the $\zeta = 2/3$ [33, 34]. However, these models also contain additional roughness exponents, $\zeta \approx 0.39$ not being one of them.

For more details on the development in this field of study, the reader is recommended the review papers [6, 7]. A collection on different mathematical tools and approaches can be found in [27].

Chapter 3

A complete description of the model used

“ Dessine-moi un mouton. ”

Antoine de Saint-Exupéry, *Le Petit Prince*, 1943

In this chapter I will present a very detailed description of the model I have been developing with my supervisor Alex Hansen and colleague Arne Stormo. We have presented and described the model to some extent in every paper included in this thesis, particularly in [18], but here I will present everything in one place. From concept to implementation, this will be the definitive collection, down to the nitty-gritty technical details.

3.1 The theory behind the model

It is always preferable to be standing on the shoulders of giants, if one wishes to reach new heights. The model we have developed has its roots in the model proposed by Batrouni et al. [5] and Schmittbuhl et al. [52]. The central concept is to take two pieces of an unspecified elastic material and connect them with lots of elastic bonds. If the binding is different from the pieces of material - let us give them a shape and call them plates - we have essentially glued two plates together. Another way to look at the situation, if you want to study fracture, is to let the bonds be of the same material as the plates. Then we effectively get a bulk elastic material with a weak plane in the middle. When this system is loaded sufficiently, a fracture will develop which will split the system down the weak plane. The idea is then that this should constrain a three dimensional fracture into two dimensions, thus greatly simplify the physics and analysis of the fracture system.

In practice, instead of realising this system, it is preferable to look at one half of this system. This entails connecting one elastic plate to an infinitely stiff plate. This, and its mirror system is an equivalent system to using two elastic plates, and has the advantage of further simplifying the model by reducing the number of variables. Additionally, it greatly simplifies an experimental setup as you can then secure one side of the material to a frame without affecting the results as one side should be infinitely stiff. Figure 3.1 shows a sketch of the system.

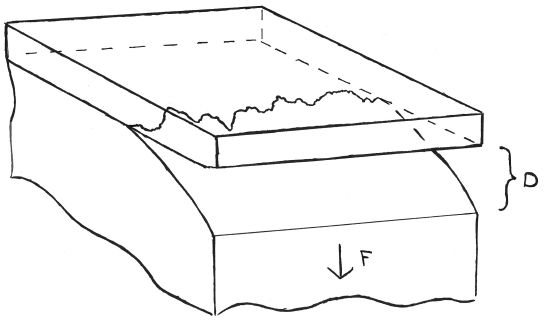

Figure 3.1: Sketch of a system used to study in-plane fracture. The experimental setup uses two plates of PMMA sintered together to create a bulk material with a weak plane. The two external control parameters are F and D, representing either force-controlled or displacement-controlled loading, respectively.

The experiment has been realised in Oslo by the research group of Måløy et al. [13, 38–40, 48, 49, 51, 53, 58], as described in the previous chapter.

Model-wise, we create a number of elastic bonds with a random distribution of breaking thresholds $t_{i,j}$ to include quenched disorder, and equations based on LEFM govern the interactions and effects of the bonds. More specifically, given a two dimensional distribution of bonds, a bond at coordinates (i, j) obeys the relation (Hooke's law)

$$f_{i,j} = -k(u_{i,j} - D), \tag{3.1}$$

between the force $f_{i,j}$ it carries and the difference between a local displacement $u_{i,j}$ and a global displacement D, with a proportionality factor k. In principle, the proportionality factor could be unique for every bond, $k_{i,j}$, but in practice all k's are given the same value simply to avoid mixing effects from disorder in both bond breaking thresholds and bond stiffness. The local displacement is caused by the behaviour of *all* other bonds and is modeled through

$$u_{i,j} = G_{i,j;m,n} f_{m,n}, \tag{3.2}$$

where $G_{i,j;m,n}$ is a Green's function and summation is carried out over repeated indices. The Green's function is dependent on the material properties ν, the Poisson ratio, and E, the Young's modulus, and is [11]

$$G_{i,j;m,n} = \frac{1-\nu^2}{\pi E a b} \int_{-a/2}^{a/2} \int_{-b/2}^{b/2} \frac{dxdy}{|\vec{r}_{i,j}(0,0) - \vec{r}_{m,n}(x,y)|}. \tag{3.3}$$

The integration is carried out over the *local* xy-coordinate system associated with and centered around (m, n), $x \in [-a/2, a/2], y \in [-b/2, b/2]$. The Green's function relates the effect of the force acting over the *area* of a single bond at (m, n) to a response at the point (i, j), effectively turning it into a two-point correlation function. In practice, and again for simplification[1], we set $a = b$. The difference $|\vec{r}_{i,j}(0, 0) - \vec{r}_{m,n}(x, y)|$ gives the distance between a point around the bond at (m, n) and the bond at (i, j).

That is really all the theory behind the model. The system is loaded either through force or displacement, and the result is calculated through (3.1)-(3.3). In the following section, the practicalities will be explained.

3.2 The implementation of the model

The model is implemented as a matrix problem on a square lattice. Starting with $L \times L = N$ bonds with a lattice spacing of a, we will end up with a linear algebra problem of form

$$\mathbb{A}\vec{x} = \vec{b}, \tag{3.4}$$

where the matrix $\mathbb{A}$ will be *positive definite*. This will be important later on. Translating equations (3.1) and (3.2) to matrix form,

$$\vec{f} = -\mathbb{K}(\vec{u} - \vec{D}) \tag{3.5a}$$

$$\vec{u} = \mathbb{G}\vec{f}, \tag{3.5b}$$

and combining, yields the result

$$(\mathbb{I} + \mathbb{K}\mathbb{G})\vec{f} = \mathbb{K}\vec{D}. \tag{3.6}$$

Now, all vectors are of length L^2 and all matrices are of size $L^2 \times L^2$, because there are in total L^2 bonds and the coupling matrix relates the response of the force at every bond to every other bond, totaling L^4 interactions. $\mathbb{I}$ is the unity matrix and $\mathbb{K}$ is a diagonal matrix where all the diagonal elements have the value k.

The $1/r$-shape of (3.3) gives rise to very long range interactions. In practice, these interactions have infinite reach, which is a problem that will be discussed later on. For now, it suffices to say that this means that we have to include all bonds in the calculations. We cannot define a ring or other set of nearest interacting neighbours, which would reduce the number of calculations needed to solve the equation set.

Equation (3.6) is already on the form of (3.4) and can be solved as it stands for either load-control (input $\vec{f}$ and solve for $\vec{D}$) or displacement-control (input $\vec{D}$ and solve for $\vec{f}$), although the former will technically involve a matrix inversion.

[1] And there really is no immediate reason to assume rectangular bonds.

The simulation starts with all bonds intact, implemented by setting all k to 1. Since all k is assumed equal, $\mathbb{K}$ doubles as a book-keeping matrix. This is done by letting unbroken bonds have a $k = 1$ and when a bond should be broken, setting the corresponding diagonal element of $\mathbb{K}$ to 0, irreversibly nullifying the load-bearing capacity of the bond[2]. An immediate benefit of this definition is that the trace $\mathrm{tr}(\mathbb{K})$ returns the number of unbroken bonds in the simulation, and a small amount of memory is spared.

For each step in the simulation, a unit global displacement $\vec{D}$ is set, and the resulting forces $\vec{f}$ acting on every bond are calculated. Then, the bonds with the highest ratio of strain to threshold is broken,

$$\epsilon = \max\left(\frac{f_{ij}}{t_{ij}}\right). \tag{3.7}$$

Note that the strain of the bond is not explicitly calculated because k can only have the values 1 or 0. The inverse of the quantity ϵ measures the actual strain due to the unitary global displacement and is used to scale the resulting total force acting on the system. In the simplest form, the simulation progresses by repeatedly solving (3.6) and breaking one bond every step until all bonds are broken and the plates are completely separated. This procedure assumes the system can be solved quasistatically, a topic I will discuss further.

The algorithm as outlined up to this point is completely solvable, but will not produce a fracture front, which is what we were looking for. So far, we have constructed two bonded parallel plates and loaded them evenly in pure global tension. The missing pieces are: specific loading conditions to obtain a frature front, how to solve the matrix equation, and how to express (3.3) in matrix form. But first, even though the statement that (3.6) could be solved as it stands is correct, doing this would be very inefficient and not feasible for large system sizes. It's time to optimise.

3.2.1 Exploiting symmetries

The first thing to note is that the Green's function (3.3) is only dependent on the distance between two points, and hence translational invariant and its discrete Fourier transform is *diagonal*. This means that instead of performing the matrix-vector product $\mathbb{G}\vec{f}$, one can do two Fourier transforms (forwards and inverse) and element by element multiplication in Fourier space instead. Equation 3.6 is then replaced by

$$(\mathbb{I} + \mathbb{K}\mathbb{F}^{-1}\mathbb{F}^{1}\mathbb{G})\mathbb{F}^{-1}\mathbb{F}^{1}\vec{f} = \mathbb{K}\vec{D}. \tag{3.8}$$

Using Fourier transforms exploits the $\mathcal{O}(N \log N)$-scaling of the transform versus the $\mathcal{O}(N^2)$-scaling of matrix multiplication.

[2]This makes the matrix $\mathbb{K}\mathbb{G}$ positive semi-definite, but the whole coupling matrix in (3.6) remains positive definite.

Another consequence of the invariance of the Green's function is that the matrix form of (3.3), $\mathbb{G}$, should also be *symmetric*, which in turn makes the entire matrix problem *positive definite*. This will have consequences dependent on what type of numerical equation solver is used. More on this in sections 3.2.2 and 3.2.4.

3.2.2 Discretising the Green's function

In order to implement the model, we we need to solve the integral in (3.3). The problem of the response of a material under a uniform pressure acting on the area $2\varepsilon_x \times 2\varepsilon_y$ was solved by Love [37]. The solution is given by

$$\begin{aligned} u_{i,j;m,n} = \frac{f_{m,n}}{4\varepsilon_x\varepsilon_y}\frac{(1-\nu^2)}{\pi E} \times \Bigg\{ & (i+\varepsilon_x)\ln\left[\frac{(j+\varepsilon_y)+\{(j+\varepsilon_y)^2+(i+\varepsilon_x)^2\}^{1/2}}{(j-\varepsilon_y)+\{(j-\varepsilon_y)^2+(i+\varepsilon_x)^2\}^{1/2}}\right] \\ & +(j+\varepsilon_y)\ln\left[\frac{(i+\varepsilon_x)+\{(j+\varepsilon_y)^2+(i+\varepsilon_x)^2\}^{1/2}}{(i-\varepsilon_x)+\{(j+\varepsilon_y)^2+(i-\varepsilon_x)^2\}^{1/2}}\right] \\ & +(i-\varepsilon_x)\ln\left[\frac{(j-\varepsilon_y)+\{(j-\varepsilon_y)^2+(i-\varepsilon_x)^2\}^{1/2}}{(j+\varepsilon_y)+\{(j+\varepsilon_y)^2+(i-\varepsilon_x)^2\}^{1/2}}\right] \\ & +(j-\varepsilon_y)\ln\left[\frac{(i-\varepsilon_x)+\{(j-\varepsilon_y)^2+(i-\varepsilon_x)^2\}^{1/2}}{(i+\varepsilon_x)+\{(j-\varepsilon_y)^2+(i+\varepsilon_x)^2\}^{1/2}}\right]\Bigg\}. \end{aligned} \tag{3.9}$$

This equation gives the deformation $u_{i,j;m,n}$ at point (i,j) due to a force $f_{m,n}$ acting uniformly over the area $a \times b = 2\varepsilon_x \times 2\varepsilon_y$ at the origin on the surface of an elastic material. In practice, we use a square lattice, so $a = b$ and $\varepsilon_x = \varepsilon_y$.

To obtain $\mathbb{G}$ is a matter of assembling a matrix from all $u_{i,j;m,n}$, which can be done in more than one way. The straightforward manner is to simply collect all terms into

$$\mathbb{G} = \begin{pmatrix} u_{1,1;1,1} & u_{1,1;1,2} & u_{1,1;1,3} & \cdots & u_{1,1;L,L} \\ u_{1,2;1,1} & u_{1,2;1,2} & u_{1,2;1,3} & & \\ \vdots & & \ddots & & \vdots \\ \vdots & & & \ddots & \vdots \\ u_{L,L;1,1} & & & & u_{L,L;L,L} \end{pmatrix}. \tag{3.10}$$

The exact ordering of the terms in (3.10) depends on whether one counts rows first or columns first. The example given is based on row-major ordering. Since the Green's function is only dependent on the distance between two points, not only is (3.10) symmetric, but the only unique elements are fount in the top line[3]. This redundancy means it is only necessary to store L^2 values for $\mathbb{G}$ instead of the full L^4, suggesting the use of an implicit solver over an explicit solver.

[3]And even these are not all unique as there are four elements an equal distance a away from any point on a periodic square lattice.

An important point about the discretisation of the Green's function is that it will determine the boundary conditions of the problem. Without a direction in the problem, bi-periodic boundary conditions are preferable. In order to develop a fracture front, we will need a direction in the problem, which makes periodic boundary conditions theoretically more suitable. However, when solving the system for very soft systems (low values of E), simple periodicity makes the equation system very ill-behaved, and one is forced to use full bi-periodicity to obtain a solution[4]. The reliability of the calculations were checked, and there is little or no impact on the accuracy of using bi-periodicity over periodicity in one direction alone. However, the run time and range of available E is greatly decreased and increased, respectively. As a result of this, we calculate $\mathbb{G}$ taking into account the closest mirror images of the system in all directions. However, the way we solve the problem, we never explicitly construct the matrix $\mathbb{G}$.

3.2.3 Loading conditions

In order to have a fracture front develop in the system, we need directionality. There are several ways this could be implemented. The two most intuitive ways would be to add some sort of gradient to either the force or displacement, whichever is controlling the system. The challenge with a loading gradient in the displacement is to choose the one which makes the most sense, physically. The challenge is similar in a load-controlled system, but then one has to solve the inverse of the matrix problem. A point loading, or loading over several points, along the edge or some curved function like $1/r$ could be relevant candidates in $\vec{f}$. In the displacement, it would make more sense with a linear gradient to emulate a driving wedge.

We chose a third option. Instead of guessing a shape for the loading in $\vec{f}$ or $\vec{D}$, we chose to implement the gradient in $\vec{t}$, the threshold distribution. The advantage of putting a linear gradient g in the thresholds,

$$t_{i,j} = gj + r_{i,j}, \tag{3.11}$$

is that in the absence of any elastic forces, the model would then be analogous to the well known *gradient percolation* model. $r_{i,j}$ is a random number drawn according to some random distribution. For all the results presented in this thesis, I have used a flat distribution between 0 and 1,

$$r_{i,j} \in [0, 1]. \tag{3.12}$$

This way of implementing the loading should be analogous to keeping a roughly constant angle of contact when separating the plates.

In the case of an infinitely stiff plate,

$$\lim_{E\to\infty} G_{i,j;m,n} = 0,$$

[4]This is not completely understood, but I assume the bi-periodic matrix is more symmetric and that this becomes important when there are large local differences in the force field.

and (3.6) and (3.8) reduce to

$$\vec{f} = \mathbb{K}\vec{D}. \tag{3.13}$$

In this limit, the model is equivalent to the equal load sharing (ELS) fiber bundle model with an imposed gradient.

3.2.4 Details on the numerical solver

It has already been mentioned that due to the long-range interactions of the elastic forces, the resulting matrix problem is initially completely dense and as the simulation progresses, the level of density is exactly $\mathrm{tr}(\mathbb{K})/L^2$. In theory, one could choose freely between a direct solver or an iterative solver. There are several numerical libraries with very efficient direct solvers for both dense and sparse equation systems. Usually, the level of efficiency is coupled to the level of density/sparsity and if there are any specific structures in the matrix. Matrices of varying density are not particularly suited for a generalised and optimalised library. During the description of the model, I have detailed several features and optimisation tricks which greatly favor an iterative solver. In practice, the iterative method I have implemented completely outperforms[5] any direct solvers I have tested. In section 3.2.1 we discovered that the coupling matrix in (3.8) is positive definite. As a consequence, the Conjugate Gradient (CG) method can be used.

Conjugate Gradient

I use a plain variant of the CG method. Some details on the CG routine is listed in [16]. It consists mainly of initialization of variables and a loop containing three vector-vector additions, two dot products and one matrix-vector multiplication. The loop goes over as many iterations are needed to obtain a given tolerance[6] level, up to a maximum of n, where n is the length of the vectors. For typical system sizes, the CG solver as implemented here converges on $\mathcal{O}(10)$ iterations. Since the solver is called once per broken bond, it is quite important to make every iteration as effective as possible.

As explained in section 3.2.1, the matrix-vector multiplication can be replaced by two Fourier transforms and effectively a vector-vector multiplication. Additionally, described in section 3.2.2, there is no need to store a complete Green's function in matrix form. Instead, we take advantage of the fact that the matrix itself is not

[5] Figuratively destroys the competition. There have been some tension in the literature on fracture models on the direct/iterative issue. The simple facts are that if you have a very sparse matrix, which you would have in most models except ours, you can use very efficient algorithms (like Cholesky factorisation) and non-standard matrix formats. If you have a very dense matrix, you can not, and your best bet would be an iterative solver. I would be very surprised by and extremely interested in a solver which outperforms the one detailed here.

[6] The tolerance is the maximum difference between $\mathbb{A}\vec{x}$ and $\vec{b}$ you will accept.

explicitly required in the CG algorithm, only implicitly through the result of the matrix-vector multiplication. Also, since the Green's function is only dependent on relative distances, all the values of $\mathbb{G}$ can be pre-calculated and Fourier transformed during initialization.

That the CG routine mostly contains simple vector operations makes it quite easy to parallelise if you can do the vector operations in parallel. A quite readily available vector machine[7] is the Graphics Processing Unit (GPU) found in most computers. The implicit evaluation of $\mathbb{A}\vec{x}$ ensures that the program is processor-bound, and not memory-bound. At least within practical limits. The vector form and dependence on processor efficiency is a great starting point for a GPU-implementation.

SBCL and CUDA

The program is written mostly in a well-maintained and efficient dialect of Common Lisp called Steel Bank Common Lisp (SBCL)[8]. To speed up the evaluation of the code, the core of the program is located in the memory of the GPU, and not the Central Processing Unit (CPU). The CPU handles flow and logic in the code, along with simple evaluations and output of data, but the real work is done on the graphics card. The interface between CPU and GPU is also an interface between code written in SBCL and code written in CUDA. This foreign function interface was written by me, and is made freely available[9]. Essentially, the code links nVidia's numerical libraries cuBLAS and cuFFT and makes them callable from the CG routine. cuBLAS and cuFFT are ideologically based on the numerical libraries BLAS and FFTW.

The parallelisation of the code is necessary in order to study large systems. Even though the fracture front itself obviously scales $< L^2$, we use a square matrix to try to minimise edge effects. This means that to increase L, we have to increase according to L^2. Early versions of the simulation code could use about half an hour to solve a single system of $L = 64$, and the runtimes would scale by about a factor 17 per doubling of L. $L = 512$ was borderline impossible, the calculation would take somewhere between three to six months. The current version is more than two orders of magnitude faster. $L = 64$ is solved in a matter of seconds, and $L = 512$ is solved in less than 24 hours. For systems less than $L = 128$, initialisation time is on the order of the total runtime (wall clock). The largest system size available, if one can wait a couple of weeks, is now $L = 2048$. The scaling is also no longer a factor 17, but it decreases slightly with increasing system size. If you can wait a month or two, or do not require a complete system (a fracture front is completely developed after about $L^2/3$), $L = 4096$ is feasible, given you have a quite modern graphics card

[7] Technically a stream processor.

[8] `http://www.sbcl.org`

[9] `http://www.github.com/knutgj`

available[10]. Further details can be found in [16]. $L = 8192$ is practically impossible, and this is not likely to change for a while. This will be discussed further in section 3.6.

3.3 Conveyor belt or treadmill?

In a normal $L \times L$ simulation, it takes about a third of the simulation before a stable fracture front has developed. The word stable seems perhaps strange in the context of a fracture process, which is usually associated with out-of equilibrium conditions. By a stable fracture I mean that the statistics of the fracture front have fully developed. At this point, the behavior of the fracture front is analogous to a Monte Carlo process with respect to the front morphology, except that the fracture process has a memory. This memory, however, is of a quite finite length. A front will typically have lost its memory after advancing between two to ten pixels. Due to this, one can extract data from more than one front per system.

During the last part of the simulation, the fracture front is subject to the boundary conditions. This definitely applies for the final 10% of the simulation, but to be completely sure, data from the last fifth to third is not used for the statistics. This means that only between a third and a half of the total simulation is useable for gathering statistics. To amend this situation, we implement a new technique.

The technique is based on the three properties:

1. the bonds break irreversibly and completely,
2. there is a predictable directionality in the evolution of the simulation, and
3. the active (process) area is less than the total matrix area.

The idea is that when the fracture front (or similar process) has passed through the material, what is behind the front is completely destroyed material, and computationally useless. The interesting area is ahead of the front, and one wishes to maximise that area. What we do in the simulation is to set a parameter ρ, which controls this level. The simulation algorithm is now changed so that with every broken bond, there is a check to see if

$$\rho > \frac{\mathrm{tr}(\mathbb{K})}{L^2}. \tag{3.14}$$

If this is fulfilled, the bottom line of the system is removed, all values are shifted down one step, and a new, statistically identical row of bonds is added to the top.

[10] nVidia's C2070 or better has enough memory to solve the system, if you can get one dedicated for the required time. GPU users are used to very high work load over short times, not very extended use. This can probably be amended though; the current version of the code has a much higher focus on speed than memory usage, and apart for in-place operations is not optimised for memory.

As a side-effect, the threshold values have to be normalised to avoid infinite forces as the system size in j-direction grows to infinity. In practice, the simulation grows from $L \times L$ to $L \times \kappa L$, where κ is an arbitrary number (in practice an integer) ≥ 1. In our case, the desire is to have the active zone as far away from the edges of the system as possible, due to the bi-periodicity, so $\rho = 1/2$. In the case of only periodicity in the front direction, ρ would be set much lower to give more space to any long-range interactions ahead of the front. An alternative approach is to implement the shift whenever a given number of the bottom rows are completely destroyed, whichever is more practical.

The effect of this is to stretch out the middle part of the simulation, so that when the total number of broken bonds in a simulation has grown larger than L^2, there is a 100% statistical yield from the computations. Instead of initialising ten systems and not using the last part of every simulation, why not initialise one system and run it ten times longer? There are two caveats that must be emphasized. Any derived parameters such as the stress and strain are affected by the shift in thresholds and the following normalisation. This must be treated with extreme care if these quantities are to be used in a statistical analysis. Secondly, the sentence on 100% yield from computation out over $L \times L$ is not strictly true. For a program running 100% on the CPU or 100% on the GPU, it is true as it stands, but for any mix, communication between the CPU and GPU steals some of this yield. This will be further explained in section 3.6.

Figure 3.2 illustrates the process. The model has been coined the conveyor belt (or treadmill) model due to the continued supply of unbroken material (or because one keeps the front running).

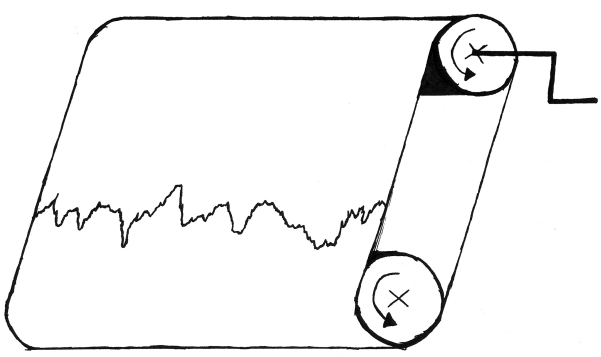

Figure 3.2: Sketch of the principle behind the steady state fracture implementation. As material becomes completely destroyed, it is removed from the simulation and new material is generated ahead of the crack, allowing for indefinite fracture propagation.

3.4 Overview of the assumptions in the model

This section will present the assumptions the model is build upon. Some will immediately be completely addressed, while some will be re-addressed in chapters 4 and 5.

Brittle fracture

No plasticity effects are available at all. All bonds break completely, irreversibly, and instantaneously as they are stretched beyond their threshold. In the context of making a simple model of fracture, I think it is perfectly valid to start with a model containing only brittle fracture. Brittle fracture is a simpler process than ductile fracture, and ductility is not needed in a fracture process.

Green's function

There are several assumptions regarding the Green's function. That the force distribution can be handled by a function, (3.3), and that the material can be implemented on a matrix is the core of the model. From the viewpoint of statistical physics, this is again a perfectly valid assumption.

The function itself is based on LEFM. That this is enough, ties in with the assumption on brittleness. Statistical physics concerns general statements on collective behavior, not precise modeling of individual behavior. This is not a molecular dynamics simulation. If LEFM turns out to be insufficient, the Green's function could be altered to include NLEFM and/or EPFM effects.

In the derivation by Love [37] of equation 3.9, there are some assumptions. Notably, that the pressure on the surface is not continuous all all points, but it its derivative is. This by itself does not seem to affect the solution of (3.8), but it does govern the validity range of the model. As long as the local gradients in (3.9) are not too great, the equation is valid. For materials with a very low E, local differences in the displacement field become very large due to the extreme softness of the material. In this domain, the assumptions behind (3.9) are no longer valid. This is directly observable in the simulations through an accuracy calculation. A re-write of (3.6) leads to

$$\vec{p}_{\text{rel}} = \frac{\mathbb{K}\vec{D} - \mathbb{K}\mathbb{G}\vec{f} - \vec{f}}{\vec{f}}, \tag{3.15}$$

and the maximum norm $||\vec{p}_{\text{rel}}||_\infty$ provides an estimate of the accuracy of the result of the CG calculation. This number sharply increases for the lowest values of E, reaching $\mathcal{O}(1)$ before the numerics break down. This is further commented in section 3.5.

Another assumption behind (3.9) is that the elastic forces have an infinite half-plane to act through. The real world experimental setup has dimensions of centimeters. The most correct estimate on the physical size of the simulations I can provide is that $aL \in \langle 0, 1 \rangle$cm, most probably on the order of a very few mm. This implies that the unit length a is on the order of μm or less, which means that the depth of the real world setup is at least a factor 1000 times a. While far from infinity, I should mean that this is sufficient not to worry about any issues due to the depth.

Weak fracture plane

Why should one study in-plane fracture when real world fractures include out-of plane effects? The idea is that it is possible to short circuit three dimensional effects and focus solely on the underlying processes of fracture front propagation in two dimensions. The working hypothesis is that in three dimensions, there are no new processes, only new, more complex effects of the same processes. This is also the idea behind the experiments performed in Oslo [13, 38–40, 48, 49, 51, 53, 58].

Quasi-static approach

The way the model is implemented carries with it some great advantages and some disadvantages. One great advantage by breaking bonds with the exact force required is that if there is a critical point in the process, one follows that critical point. The necessary accompanying disadvantage of jumping directly to the required force is that there is no direct concept of time, and thus no time for dynamic processes such as stress waves and information delay. In the current model, the speed of sound in the material is technically infinite and stress waves cannot form.

Boundary conditions & finite size

Due to the long-range elastic interactions, it is desirable to have a large as possible L. I have already explained how the edge effects are present and how they effectively reduce the available size of the model, though this can be minimised in some extent through ρ. It is also possible to construct a $\mathbb{G}$ that reduces or eliminates these effects, though at a cost of loss of periodicity. For very large L, this would of course be preferable, but for the range of available L, some form of periodicity is needed to reduce finite size effects from the long-range interactions. In this work, only the nearest mirror images have been taken into account. The calculations behind $\mathbb{G}$ can be improved to take into account higher order mirror systems.

Then there is the apparent problem with having forces with infinite reach within a finite boundary. I use the word apparent because I consider this situation completely analogous to an edge crack under uniaxial loading in an ideal material, where the

stress has a finite but non-zero value at every point in the sample, σ_∞. The importance is not in the value of σ_∞ per se[11], but in local variations higher than σ_∞. The argument is essentially that as long as this level is not too high but it still covers the entire simulation area, it can be treated as uniform stress potential and safely ignored, as the absolute level of a potential should not affect the physics, only the difference in potential is important.

An additional effect of the infinite reach which actually is a problem, is the backwards reach of the interactions. The fracture front is always moving upwards in the simulations, so the bottom part consists entirely of broken bonds. Due to the bi-periodicity, this could also be considered a fracture front which would be propagating downwards. If this should happen, this front would loop around and come in from the top of the simulation, which would then be *ahead* of the proper fracture front. This would ruin the simulation, and is the reason for keeping the fracture front in the middle of the sample ($\rho = 1/2$). One way to avoid this situation is to limit the lower range of E. A stiffer system is more controlled by the quenched disorder in the threshold distribution (see next section), which is always increasing upwards, making it difficult to loop around. This is not desirable in general, as we want to study the fracture front in the limit of large elastic interactions. It is the elastic stress concentration in this regime that can cause the undesired loop-around. To counter this effect, one can artificially increase the thresholds at the very top of the system, creating a barrier that is stronger than the stress concentration. As long as the proper fracture front in the middle of the sample is far enough away not to interact with this barrier, this countermeasure will not affect the rest of the simulation. Since the barrier is in the thresholds, and not in any force distribution, interaction means that the proper fracture front will have to try to break a bond in the barrier. If this should happen, it would mean that the fracture front is so close to the edge of the system that boundary effects are already in play and the data from the simulation should not be used in any case. The bottom line is that the barrier implementation ensures that only one fracture front is moving through the sample without interfering with the fracture process.

3.5 Control parameters

As it will turn out, there are primarily two control input parameters in the model,

$$e \equiv Ea/L \tag{3.16}$$

and g. Both are freely tunable, but limited by physics in different ways. The gradient g controls the range of possible interactions, and is analogous in some respects to the stress-intensity factor K, but g controls the situation differently. A high stress-intensity factor translates to high stress gradients near the crack tip, resulting in

[11] Given σ_∞ is not high enough to initiate other fracture processes.

(probably) a lot of fracture events close to the crack tip. A very low K would differentiate much less between stresses close to and far away from the crack tip. A low K could mean either a very slow, creep-like loading, or a very rapid loading of the entire sample such that all bonds are loaded approximately equally at the same time. Similarly, a high g will favour fracture events close to the front, and in the limit of vanishing gradient, the entire sample is uniformly loaded.

An alternative way to visualise g is to imagine a tilted plane between the two loaded plates. The tilt is equal to g and in the j-direction. At some point, there will be a lowest possible threshold which has not broken yet, given by $t^{\min} = gj^{\min} + 1$. A distance r_g ahead, there will be a value approximately equal, and the one farthest away is $t^{\max} = gj^{\max} + 0$, such that the difference between $t^{\max}$ and $t^{\min}$ corresponds to r_g. This r_g represents the "field of vision" or active zone or simply the range of interactions due to randomness alone. One can define

$$r_g = \frac{1}{g} \equiv L', \tag{3.17}$$

which is the effective size L' of the equivalent gradient percolation system $(L \times L')$.

The practical range of g is partially given through (3.17) so that

$$\frac{1}{g} \in [3, L + \lambda]\text{pixels}, \tag{3.18}$$

where λ is a number dependent on E. The effect of the Green's function has to be sufficiently strong to result in stress concentration powerful enough to constrain the active zone so that $L' - \lambda < L$. The lower limit of 3 pixels is a number set low enough to be valid for most values of L and E. In practice, this number depends on the roughness exponent and has to be high enough to allow a fracture front to completely develop.

The parameter e can considered an effective Young's modulus and connects the discretisation, size and elasticity. Relation (3.16) dictates how one can compare systems of different L and E, and in principle a, but this parameter has not been considered a variable. The reason is again to simplify the analyses and to focus on the variables of more immediate interest.

In practice, e tunes how active the Green's function is, with a low value for e corresponding to strong elastic interactions. Through (3.16) we end up coupling low e values to high elasticity, i.e., a very soft material, or a large length scale. And vice versa. The relation also explains how a simulation with a large L and a global E at a given level can have different behavior at different length scales $\ell < L$ because the effective modulus will have a range $E/L < E/\ell < E$.

As already mentioned, e has a lower bound because the assumptions behind (3.9) become invalid when E is too low. There is no upper bound on E. The consequence of an infinite E is a vanishing Green's function, as explained in section 3.2.3. On

a computer, this can be realised without actually changing (3.8) to (3.13) if using high enough precision. However, in optimising for speed and running on a GPU, it suffices with single precision floating point numbers, which puts a constraint on the range of e. Thus, the effective range of e is

$$e \in \left[10^{-6}, 10^{5}\right], \tag{3.19}$$

for $L < 1024$. For larger systems, the limits could be pushed slightly further.

3.6 Future improvements to the model

The biggest issue with the current version of the simulation code is the communication between the processor (host) and the graphics card (device). Examples of data transfer speeds are host-to-device at 1.8GB/s and device-to-device at 17GB/s (the specifc numbers are from a GeForce GT 120 GPU). Device-to-host communication is is usually on a par with the host-to-device bandwidth, but it can be slightly slower (1.5GB/s in this example). This means that communication issues can very quickly become a bottleneck unless everything is handled on the GPU. This also applies when programming for multiple GPUs. The most time-consuming process in the current simulation code is the reporting back to the logic-controlling CPU of the single number resulting from a dot product calculation on the GPU. One obvious, but time-consuming, improvement to the code would be a restructuring of the code to run 100% on one or possible more GPUs, or on a massively parallel computer.

Another improvement could be to use a preconditioner matrix $\mathbb{Q}$. Equation 3.8 would then become

$$\mathbb{Q}(\mathbb{I} + \mathbb{K}\mathbb{F}^{-1}\mathbb{F}^{1}\mathbb{G})\mathbb{F}^{-1}\mathbb{F}^{1}\vec{f} = \mathbb{Q}\mathbb{K}\vec{D}. \tag{3.20}$$

Some time has been spent on finding a suitable $\mathbb{Q}$, but no good candidate has been found.

With regards to improvements to the actual model, not the implementation, I have several ideas. Simple additions could be to investigate the effect of micro-fractures or heterogeneities by including some pre-broken bonds or introduce some very short-range correlations in the threshold distribution. Thermal noise is also something that could trivially be included in the model.

More complex improvements could be to include plasticity through the Green's function and changing the break-down behavior of the bonds. A different loading scheme (using $\vec{f}$ or $\vec{D}$) could also be worth investigating, though Tallakstad et al. [58] reported little or no effect on the fracture process from very different loading conditions. Undoubtedly the most interesting improvement would be a generalization to full three dimensions. This is far from trivial and will require some thought.

Chapter 4

Morphostatic results

> *To see a world in a grain of sand, and a heaven in a wild flower; hold infinity in the palm of your hand, and eternity in an hour.*
>
> William Blake, *Auguries of Innocence*, 1863

4.1 Main findings

Figure 4.1 shows the stress-strain relationship from one of the simulations. The red curve shows the progression of a sample as it is loaded until it reaches a maximum stress $\sigma_{\max}$ at the strain $\epsilon_{\max}$. After this point, the sample cannot support more load, and any further increase in strain simply pulls the sample apart. The blue curve shows the progression of a sample under steady state loading. The position of the looping stress-strain level on the curve is controllable through the parameter ρ as described in Section 3.3.

Two regimes

The model contains several different behaviours, primarily dependent on the two parameters e and g. As described in section 3.5, each of these parameters has its own range. Varying e across its range from high to low is equivalent to fading-in the effect of the Green's function. Starting at a threshold dominated bond-breaking process, one ends up in a situation where the elastic forces are completely in control and the thresholds are inconsequential. In the high e-range, bonds are randomly selected to break according to their thresholds, resulting in a "damage cloud" of size $L \times 1/g$. The fracture process is constrained to this band, and everything behind this

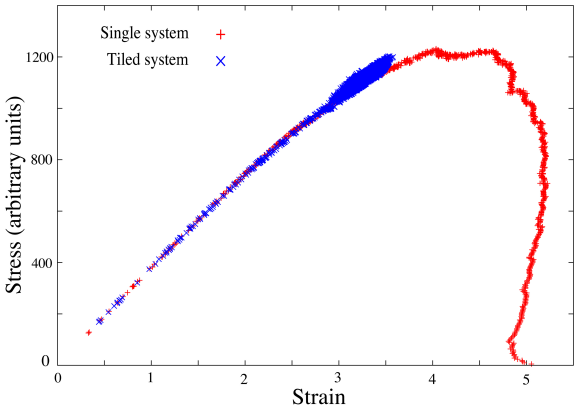

Figure 4.1: Stress-strain relationship from a simulation showing the looping of the stress-strain relationship due to the renormalisation during the steady state algorithm.

band is completely broken material while everything in front is completely unbroken material. The front advances by damage originally ahead of the front coalescing to be a part of the front. To analyse this situation, we first filter away damage not connected to the front. This amounts to ignoring single or small clusters of broken bonds, effectively locating the largest spanning cluster. A typical image of what is left is shown on the left part in Figure 4.2. To analyse the front scaling, the overhangs have to be removed. This is done using a solid-on-solid (SOS) approach. The results presented here are obtained using a first hit from above method, but tests show no difference in using first hit from below.

Figure 4.2: Snap-shots of fracture fronts from the simulations. The view is as seen from above in Figure 3.1. Black represents broken material and white is undamaged material. The left hand side shows small scale behaviour and the right hand side shows large scale behaviour. The fracture grows upwards.

The right hand side of Figure 4.2 shows a typical fracture front from the low e-range. Damage formation is now completely constrained to the front. As is visible in the figure, overhangs can form also in this regime, but they are much smaller and rarer than for high e. The SOS approach is used to remove these when necessary. For the lowest values of e, there are no overhangs.

The two regimes described is referred to as “stiff” material or small scale for high e, and “soft” material or large scale for low e. Front propagation by damage coalescence is the driving mechanism in the former case and damage formation directly on the fracture front is the driving mechanism in the latter. The intermediary range, from

low to high e, is characterised by damage beginning to form ahead of the fracture front, immediately followed by a roughening of the front.

To estimate the roughness exponent, we do a wavelet analysis of the front data. This entails calculating the average of the wavelet coefficients $W(a) = \langle |w(a,b)| \rangle_b$, which, for a self-affine signal, should scale as [24, 43, 56]

$$W(a) \sim a^{\zeta+1/2}. \tag{4.1}$$

The data for a soft system is shown in Figure 4.3. In the main figure, a power law relationship is found with an exponent $\zeta + 1/2 = 0.89 \pm 0.04$. The data in the inset contains only information on whether the front moves up or down, not how far. In other words, the jump size distribution is removed. This was done in connection to the discussion of self-similarity versus self-affinity, and will be explained in the next section. For this data, the exponent is $\zeta + 1/2 = 0.99 \pm 0.04$. The data have been scaled with the gradient to an exponent of α and β. Using the gradient percolation connection, we will calculate these exponents in the stiff regime in the next section. The exponents are included here as well for completeness.

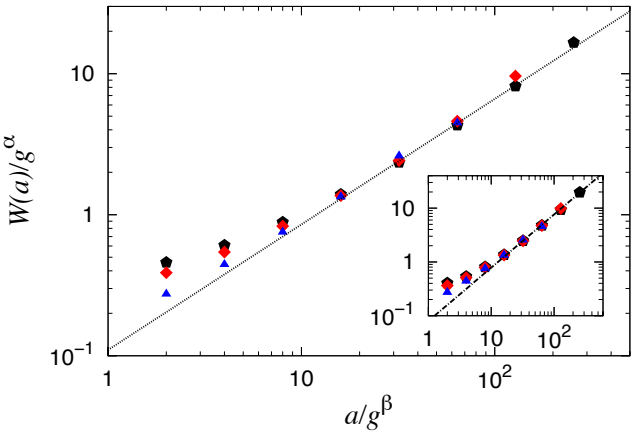

Figure 4.3: Wavelet data from systems in the soft regime. $L = \{128, 256, 512\}$ and $e = 2.44 \cdot 10^{-4}$ for the smallest L and $7.8125 \cdot 10^{-4}$ for the two larger L. The scaling exponents α and β are both 0. The slope in the main figure is 0.89 and in the inset 0.99.

For a stiff system, the situation is much different. The data is shown in Figure 4.4. Linear regression suggests a power law with an exponent $\zeta + 1/2 = 1.07 \pm 0.10$. The data in the inset will be discussed shortly.

Next, we examine the fractal dimension of the fracture front. Figure 4.5 shows the number of bonds in the front l, scaled by L^{η}, as a function of e. l is counted using a walker algorithm which traverses the interface between broken and unbroken material on the SOS front. The main figure shows data collapse for $\eta = 10/7$ for stiff systems, and the inset shows data collapse for $\eta = 1$ for soft systems.

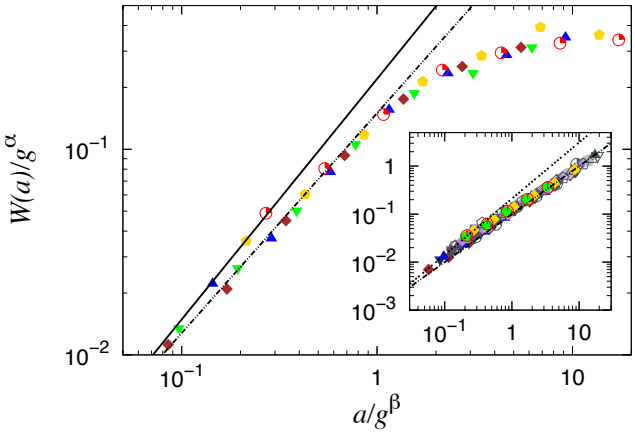

Figure 4.4: Wavelet data from systems in the stiff regime. $L_{\text{main}} = 256$, $L_{\text{inset}} = \{64, 128, 256, 512\}$ and $e = 3.125$. The scaling exponents in the main figure are $\alpha = -6/7$ and $\beta = -4/7$. In the inset, $\alpha = -2/3$ and $\beta = -4/7$. The slopes in the main figure are 1.17 and 1.07, and in the inset 1.17 and 1.00.

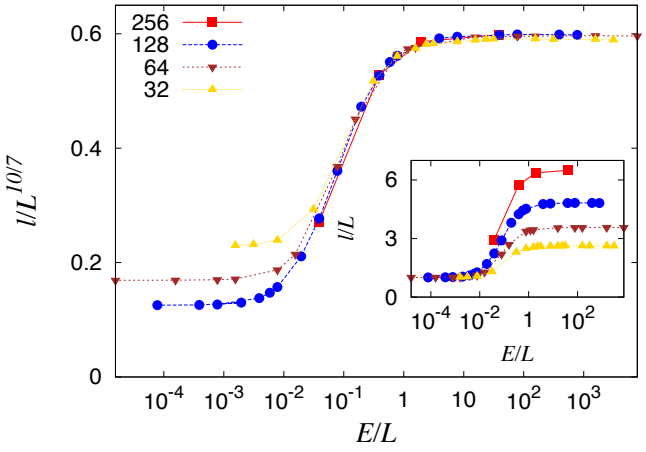

Figure 4.5: Scaling of the fractal dimension of the front for four values of L. l is the *mass of the length* of the front, or the number of broken bonds in the front. The main figure show data collapse for high e with the exponent $10/7$, and the inset shows data collapse for low e with the exponent 1.

Sample sizes

Typical sample sizes are in the thousands and tens of thousands or more for $L = 32$, and hundreds and thousands for $L = 64$. For $L = 128$, the samples number in the hundreds and sub-hundreds. Above this, each simulation is on the order of minutes, hours or more; so for $L = 256$, the sample size is usually in the range of tens. Typically in the fifties, but some data series go into the hundreds. The largest size used for statistics, $L = 512$, have a sample base of ten or less. Singular, or very few systems of sizes $L = 1024, 2048$ have been produced, but data from these have not been published. The data is spread with regards to being stand-alone systems or a tiled conveyor system for historical reasons[1]. From each of these systems, dependent on L, a number of fronts are extracted.

4.2 Evaluation and discussion

This section will discuss the results presented in the previous section and argue why the results show $\zeta = 0.39$ and $\zeta = 2/3$ even though the immediate impression from figures 4.3 and 4.4 yields

$$\zeta_{\text{soft}} = 0.39 \quad \text{and} \quad \zeta_{\text{stiff}} = 0.57. \tag{4.2}$$

The results presented so far have primarily been dependent on e because the parameter g is in a sense less important. Its value is determined after all other simulation parameters are decided, and it is set such that $1/g$ is large enough that the fracture front can completely develop, and small enough to keep boundary effects to a minimum. As long as g is in this range, it does not seem to affect the physics in the model in any way. This is experimentally supported by [58], who studied a range of loading conditions without finding any difference in the results. Section 3.5 explained how g is coupled to the loading of the system.

The effect of stress concentration is implicitly on display in Figure 4.3. $\alpha = \beta = 0$ implies that as long as the gradient is in the range just described, the shape of the front is independent of g. This applies only for soft systems as there is no stress concentration in stiff systems.

For stiff systems, we expect a connection to gradient percolation at some point. In Figure 4.4 the data demonstrates a crossover to uncorrelated noise for large a. Uncorrelated noise has a roughness exponent $\zeta = -1/2$ which seems to be the asymptotic behaviour [28]. One should expect this crossover to happen at the correlation length ξ in the system. If the correlation length is the same in both i and j-directions, and if the system behaves as in gradient percolation, one should expect $\xi \sim g^{-\nu/(1+\nu)}$, where $\nu = 4/3$. Thus, data collapse in Figure 4.4 should occur

[1]The scripting used to produce large sample sets was completed before the conveyor method was implemented.

for $\beta = -4/7$, exactly as observed. A similar argument leads to $\alpha = 3\beta/2 = -6/7$ [20, 25], again in agreement with the figure.

In order to further study the roughness of the front, we transform the height function $h(i)$ according to [25]

$$h_k(i) = \sum_{m=0}^{i} \mathrm{sgn}[h(m+1) - h(m)]|h(m+1) - h(m)|^k. \tag{4.3}$$

$h_1(i) \equiv h(i)$, and $h(i) \to h_0(i)$ removes all height information from the steps, leaving only the width of the front as caused by correlations in the sign changes, i.e., up or down movement only. This is the function behind the wavelet analysis in the insets of Figures 4.3 and 4.4. For soft systems, this analysis resulted in $\zeta_0 = 0.49$, higher than the expected $\zeta = 0.39$. This is simply due to the fact that for $h_0(i)$, the measured roughness exponent is [24, 26]

$$\zeta_0 = \max\left(\zeta, \frac{1}{2}\right). \tag{4.4}$$

For the stiff systems, the results of the transformation is a scaling of $\zeta = 0.67$ for smaller a and a transition to $\zeta = 0.5$ for larger a. The value $1/2$ is expected as white noise becomes random walk as $h(i) \to h_0(i)$. From Family-Vicsek scaling, we expect

$$\alpha = (\zeta + 1/2)\beta. \tag{4.5}$$

Again, $\beta = -4/7$ as this exponent should be unchanged by the transformation. If this system behaves as gradient percolation, the roughness exponent should be exactly $\zeta = 2/3 = 0.\overline{66}$ [25]. This again leads to $\alpha = -2/3$, which agrees with the figure.

Finally, to verify if the stiff systems indeed behave according to gradient percolation, the fractal dimension of the front D_f is examined. The number of elements in the front, l, should scale in d dimensions according to

$$l(L) \propto g^{-\psi} L^{d-1}, \tag{4.6}$$

with $\psi = (D_f - d + 1)\nu/(1 + \nu)$ in site percolation [21, 50]. In two dimensions, the exponents are exactly known, and $D_f = 7/4$, leading to $\psi = 3/7$ [21, 50]. With $g = 1/L$, the end result is $l(L) \propto L^{10/7}$. Using this scaling relation, very good data collapse is seen in Figure 4.5 for high e and most of the transition regime. The lower end of the transition and the lowest values of e obeys $l(L) \propto L$, which is to expect for a fluctuating elastic line without overhangs [27].

The scaling of the fractal dimension is very strong evidence for a percolation behaviour, indicating an exact roughness exponent of $2/3$. This is supported by the scaling of Figure 4.4, in particular the inset. Translating between elasticity and

length scale through (3.16), the results of the front analysis thus strongly indicate two regimes with roughness exponents

$$\zeta_{\text{large}} = 0.39 \quad \text{and} \quad \zeta_{\text{small}} = \frac{2}{3}. \tag{4.7}$$

However, Figure 4.4 illustrates how little it takes to measure a lower exponent of $\zeta_{\text{small}} \approx 0.6$. Fortunately, the link to gradient percolation through the indirect loading scheme and the quality of some of the data collapses permits the evaluation of exact values of the scaling exponents.

The preliminary conclusion is thus that the model contains two regimes with two different roughness exponents corresponding to different length scales $\zeta_{\text{large}} = 0.39$, due to elastic interactions, and $\zeta_{\text{small}} = 2/3$, due to random selection. This was first presented in [20].

Chapter 5

A study of the dynamics in a quasi-static model

> *Always in motion, the future is.*
>
> Yoda, *The Empire Strikes Back*, 1980

This chapter will address results connected to the dynamics of front evolution and the local fracturing process. The results are also presented in [17, 19].

5.1 Steady state fracture

Using the conveyor belt principle, the fracture front can be driven indefinitely, as explained in section 3.3. To study the evolution of the front, one can plot the width of the front w expressed as the standard deviation

$$w = \sqrt{\frac{1}{L-1}\sum_{i=1}^{L}[h_{\mathrm{rel}}(i) - \langle h_{\mathrm{rel}}(i)\rangle]^2}\ , \tag{5.1}$$

where

$$h_{\mathrm{rel}}(i) \equiv h(i)|_{t=\tau} - h(i)|_{t=\tau_0}\ . \tag{5.2}$$

Remember, the model is quasistatic, so time is not clearly defined. The most intuitive clock in the model is the breaking of bonds, as exactly one bond is broken every time the simulation advances. Thus $t \in [0, \kappa L^2]$ uniquely determines simulation progression. Taking $t = \tau_0$ at some point $t > 0$ where a front has completely developed and $t = \tau > \tau_0$ at some later point, w describes the widening of the front as developed from an *initially rough* front configuration.

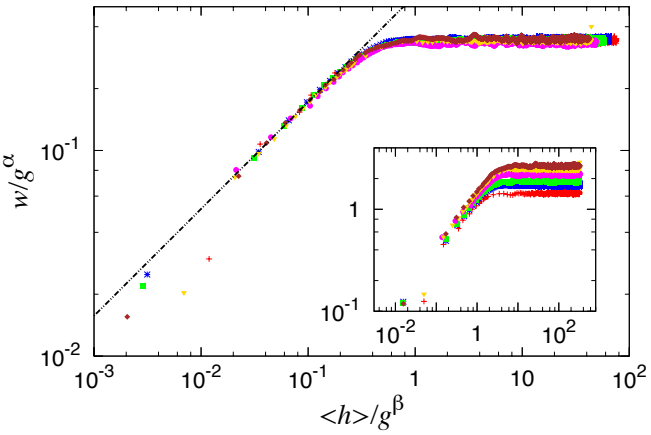

Figure 5.1: One-parameter scaling of w as a function of $\langle h \rangle$ with g as the scaling parameter for a soft system. The main figure shows data collapse for $\alpha = \beta = -0.4$. The inset shows unscaled data, i.e. $\alpha = \beta = 0$. The parameter values are, from top-down in the inset, $g \in (0.007, 0.008, 0.01, 0.015, 0.02, 0.03)$. The system size is $L = 64$. The dotted line has a slope of 0.52.

Figure 5.1 shows how w develops as a function of the average position of the front for a soft system. Note that the front matures to a constant w quite quickly. This behaviour is what is meant when using the term steady state fracture, and it shows that fronts extracted using the conveyor belt technique are statistically independent if the average position of the front has advanced about 10 pixels between each extraction.
The scaling exponents α and β seem to be equal at a value -0.4. This will be discussed shortly. A best fit to a straight line during the roughening yields a growth exponent $w \sim \langle h \rangle^b, b = 0.52 \pm 0.05$. Family-Vicsek scaling leads to the relation

$$z = \frac{\zeta}{b} \tag{5.3}$$

between the dynamic, roughness, and growth exponents [4, 14]. From this relation, we can calculate the value for the dynamic exponent to be $z = 0.75 \pm 0.1$. This value has to my knowledge not been measured experimentally[1].

Figure 5.2 illustrates the effect of the interplay between stress concentration and threshold gradient on the front. The figure shows systems with actual size $L = 64$ and effective sizes $1/g$ in the range from 16 to 200. Notice that for the largest g, the system is too constrained to let a fracture front freely develop. As g is decreased, there is a plateau between $\approx L/2$ and $\approx 2L$ where $w/g^{-0.4} \approx$ constant. As g is further decreased, damage begins to form ahead of the fracture front as the effective system size is now greater than the range of the stress concentration. When this occurs, weaker bonds further ahead are broken before stronger bonds on the

[1]The corresponding *out-of*-plane exponent has been reported to be $z \approx 0.8$ [7].

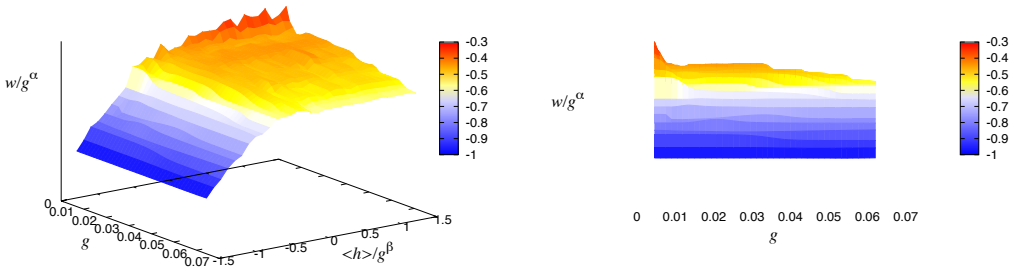

Figure 5.2: 3D view of Figure 5.1, with a greater range of g. Details in the text.

front is broken due to the increased local stress. This signifies a change in fracture mechanism and a departure from the regime where the fracture front is determined by the roughness exponent $\zeta_{\text{large}} = 0.39$. Not unexpectedly, the value of α sharply increases in magnitude from -0.4 as g approaches 0.

The corresponding steady state growth analysis for stiff systems is presented in Figure 5.3. This time the scaling exponents are $\alpha = \beta = -4/7$ and $b = 0.45$. The data are from systems with $e = 3.125$, almost at the top plateau in Figure 4.5, indicating a fracture process strongly affected by the disorder in the thresholds. With such a weak influence from the Green's function, a strong similarity to the ELS scheme is expected. The colored points in Figure 5.3 are from our model, and the black lines are obtained using ELS. The lines follow the points very closely.

The width w is independent of L, and only depends on g. Each colored group consists of data from systems with constant e and $L = (64, 128, 256)$. The inset shows how the unscaled data clearly differentiates between different g alone. Note also how as g decreases, the scatter of the data points increases. This is merely a confirmation that as the front widens, so does the statistical variations.

The observant reader is probably wondering about the range of g in Figure 5.3. Yes, the lower range could be extended further, and no, the highest g should not be included. In the gradient percolation analogy, this specific system has an effective size of $L' = 2$. It is only included to illustrate the robustness of the scaling relations. Even for an impossibly small system, a measurable signal which behaves identical to the other systems, with respect to the scaling, can be extracted. This is very different from the case of soft systems, which require a more sensible L' to show correct scaling behaviour. The most plausible explanation is that this is due to the range associated with the elastic forces. The disorder in the thresholds does not have such a range dependency and should be equally active for all system sizes.

Again, using the link to gradient percolation, one can derive that in the growth phase, the front width scales as [19]

$$w \sim \langle h \rangle^{288/637}. \tag{5.4}$$

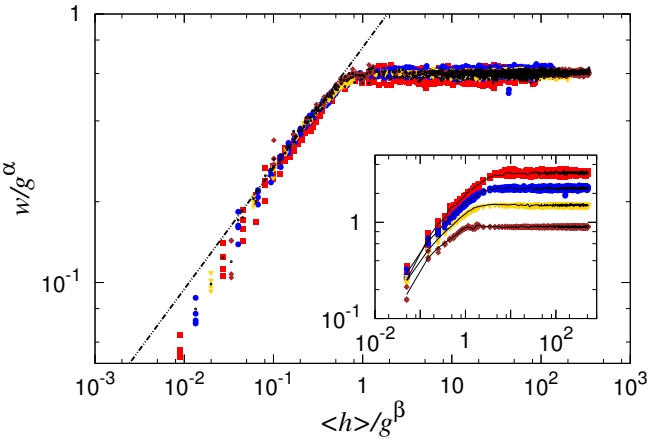

Figure 5.3: One-parameter scaling of the standard deviation of the width of the front as a function of the average position of the front as the front moves forward from some initial (rough) configuration for a stiff system. The main figure shows data collapse for $\alpha = \beta = -4/7$, and the inset shows the same data with no scaling, i.e. $\alpha = \beta = 0$. The data are extracted from simulations with, from top-down in the inset, $g \in (0.05, 0.1, 0.2, 0.5)$. Results for an equal load sharing process with the same set of gradients is included in black. Note that these results exactly match their respective counterparts. Each group in the inset is comprised of data from systems of sizes 64-256 with constant E/L. The dotted line has a slope of 0.45.

$b = 288/637 \approx 0.45$ is in good agreement with the data in Figure 5.3.

Gradient scaling exponents α and β

Due to the link with gradient percolation through our definition of g, the scaling arguments derived by Hansen et al. apply [25]. The argument is that w should scale with the correlation length ξ, which again scales as the gradient to the correlation length exponent,

$$w \to w/\xi \sim w/g^{-\nu/(1+\nu)} = w/g^{\alpha}. \tag{5.5}$$

Additionally, we expect that the accumulation of damage should increase proportionally to the width of the damage zone. This implies that $\langle h \rangle$, which is a measure of broken bonds, should scale as w, i.e., with the same exponent. This is in very good agreement with the figure, where all the data is scaled by $\alpha = \beta = -\nu/(1+\nu) = -4/7 \approx -0.57$ and data collapse is observed.

Assuming the argument for the scaling of the stiff system is transferrable, one could calculate an apparent correlation length in the soft regime to be $\nu_{\text{app}} \approx 2/3$. Another possibility is that there is no correlation length and the only length scales in this regime is the grid size a and system size L. Inspired by the analogy to gradient percolation, one could make the connection

$$w \to w/g^{\alpha} = w/\left(\frac{1}{L'}\right)^{\alpha} = w/L'^{-\alpha}. \tag{5.6}$$

In this context, $-\alpha$ could be considered a local roughness exponent with the value 0.4, in agreement with the expected value $\zeta_{\text{large}} = 0.39$. This could also explain why, for the stiff systems, the direct wavelet analysis showed indications of a small scale roughness exponent $\zeta = 0.57$ as well as the result expected from randomness alone, $\zeta_{\text{small}} = 2/3$, visible in the scaling relations.

5.2 Velocity clusters

The waiting time matrix (WTM) method [38, 58] is a technique developed to analyse experimental data in image form. The method can be directly applied to the data from our model, which is easily expressed as a binary matrix. The essence of the method is to let the fracture front traverse across a blank slate. At every time step, set a mark where the fracture front is. Once the front has traversed the entire slate, one is left with a high number of marks where the front spent a lot of time, and a low number where the front quickly passed. The difference between the experimental and numerical situation is that when translating between the local waiting times $W(i,j)$ and local velocities

$$V(i,j) = \frac{1}{W(i,j)}\frac{a}{\Delta t}\ , \tag{5.7}$$

the pixel size a and time between image frames Δt are experimentally available, but our model contains no explicit time. Again, we use the breaking of bonds as a clock, setting $\Delta t = 1$. With a time step of unity, all events are included, and the data is easily scaled if a connection to a physical time is found at a later date. The method is explained in detail in [58].

From $V(i, j)$ one can construct maps over the local velocities and calculate the global average velocity $\langle v \rangle$. In these maps, one finds clusters corresponding to areas covered by the propagation of the fracture front in relative short or long time. These clusters are called velocity clusters and are different from standard clusters in similar problems which is defined by the collection of bonds[2] breaking without a further increase in the global load. Two regimes are defined, a *pinning* regime where all the local velocities are lower than the average velocity and a *depinning* regime where all local velocities are higher than the average. Clusters in these regimes are coined pinning and depinning clusters, respectively. The pinning clusters have a snake-like physical appearance, while the depinning clusters have an elephant-in-snake-like appearance [12]. The visual similarity between clusters from our model and experimentally obtained clusters is striking [19, 58].

To each cluster there is associated a size S, which is the total number of bonds included in the cluster, and a linear size parallel and perpendicular to the fracture front, l_x and l_y. l_x and l_y are estimated by a bounding box [19], and are expected to follow the relation

$$l_x l_y \propto S \ . \tag{5.8}$$

It has been found that l_x and l_y obey the scaling relation

$$l_y \sim l_x^H \ , \tag{5.9}$$

with the exponent H in the range $[0.39 - 0.66]$ [8, 19, 36, 38, 58]. It has also been proposed that the local scaling exponent H is another measure of the roughness exponent ζ [8, 17, 19, 36, 38, 44, 58]. In this thesis and a recent paper [17], I propose that the large scale and small scale roughness exponents are signatures of different fracture mechanisms. Coupled with the evidence that there is a crossover region between these two mechanisms [20, 57], it follows that H is not necessarily another measure of ζ directly, but that the set of possible values for H is the same as the set of possible values of ζ,

$$\{H\} = \{\zeta\} \ . \tag{5.10}$$

Figure 5.4 shows the relationship between l_y and l_x primarily for a soft system, where the measured roughness exponent is $\zeta_{\text{large}} = 0.39$. Due to the limited sizes of the simulations, a filtering has to be introduced. This filtering was originally introduced in the experiments, but there the results seem to be independent of the

[2] Or fibers, fuses, etc.

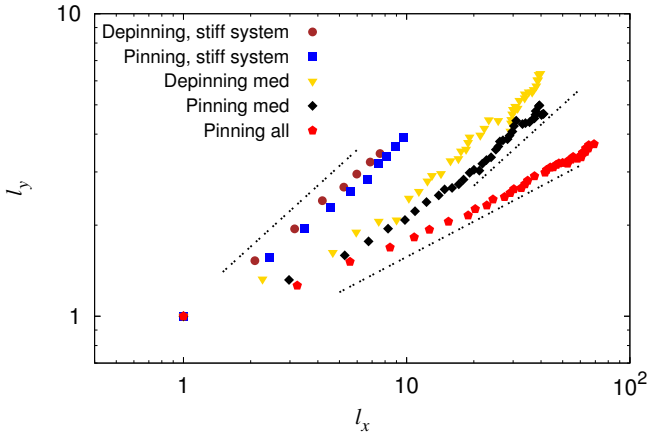

Figure 5.4: Local scaling of the clusters. The lines are guides to the eye, but the slopes are based on linear regression and the values are in descending order 0.67, 0.67, and 0.39. The data labeled stiff system are from simulations using a Young's modulus four orders of magnitude greater than what is used in the rest of the simulations. Further details in the text.

filter parameter [58]. The dependence on this filter in the simulations is purely a size effect [19]. In the pinning regime, one finds $H_{\text{pin}}^{\text{all}} = 0.39 \pm 0.03$ if *all* velocities below and equal to $\langle v \rangle$ are included in the cluster map. If the velocities closest to and equal to the average velocity are not included, one finds $H_{\text{pin}}^{\text{med}} = 0.67 \pm 0.06$. If a high filter is set, to include only the lowest velocities, there is not enough data left to determine $H_{\text{pin}}^{\text{high}}$ due to the relative small size of available system sizes. In the depinning case, only a medium filter gives sensible results, which is again a finite size effect. All velocities cannot be included, because the result is typically one giant cluster spanning the entire system, and a few very small ones if there is any space left. This situation skews the statistics so no data can be extracted. At the other end, if the velocity filter is set too high, much of the data is filtered away and there seems to be a loss of structure [19]. If only the values closest to $\langle v \rangle$ is dropped[3], the result is $H_{\text{dep}}^{\text{med}} = 0.67 \pm 0.05$. A further discussion on the velocity dependence is given at the end of this chapter.

Should the hypothesis (5.10) be correct, one would expect that by changing the system parameters so that the measured roughness exponent changes, the measured H could also change. Indeed, this effect is visible in Figure 5.4 in the two data series labeled "stiff system". These data series are from a simulation with a Young's modulus which is five orders of magnitude greater than the other systems, placing the system in the stiff region and thus $\zeta_{\text{small}} = 2/3$. Here, neither pinning nor depinning clusters show any trace of the 0.39-scaling and $H_{\text{pin}} = H_{\text{dep}} = 0.67$.

The probability distribution of cluster sizes has also been studied [8, 19, 36, 38, 58],

[3]Again, this is absolutely necessary due to the finite system size.

and showed to be on the form

$$P(S) \sim S^{-\gamma}. \tag{5.11}$$

Similarly, the probability distributions of l_x and l_y are [19, 58]

$$P(l_x) \sim l_x^{-\beta_x} \quad \wedge \quad P(l_y) \sim l_y^{-\beta_y}. \tag{5.12}$$

Tallakstad et al. investigated the individual scaling of l_x and l_y with respect to S and found power laws of the form [58]

$$l_x \sim S^{\alpha_x} \quad \wedge \quad l_y \sim S^{\alpha_y}. \tag{5.13}$$

These relations were also found in our model, and the results are presented in Figure 5.5 [19]. With the lesson learned from the size and velocity "dependence" in Figure 5.4, the data in Figure 5.5 are from the groups showing the clearest scaling relations, so depinning data does not include the velocities closest to the average velocity, and pinning data includes all velocity data. Measured values are given in the figure and uncertainty estimates are given in the figure text.

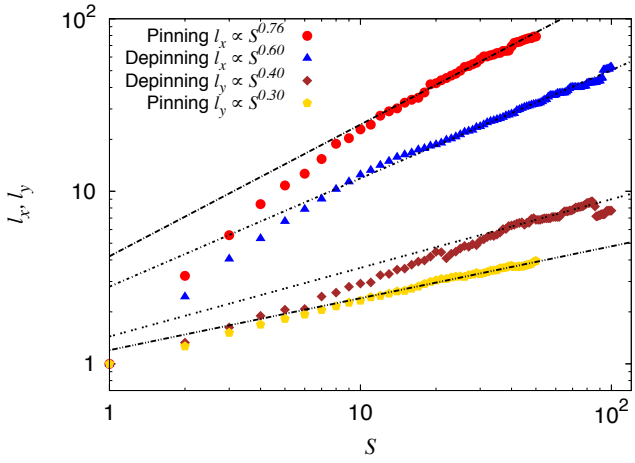

Figure 5.5: Linear size of both pinning and depinning clusters as a function of cluster size. The measured exponents are in descending order: 0.76 ± 0.05, 0.60 ± 0.04, 0.40 ± 0.08 and 0.30 ± 0.04.

Eliminating S from (5.13) and comparing with (5.9) leads to the relation between the exponents

$$H = \frac{\alpha_y}{\alpha_x}. \tag{5.14}$$

The data in Figure 5.5 are in close agreement with $H_{\text{dep}}^{\text{med}}$ and $H_{\text{pin}}^{\text{all}}$.

Combining (5.8) and (5.9), one can define

$$S = f(l_x) \sim l_x^{1+H} \quad \wedge \quad S = g(l_y) \sim l_y^{1+\frac{1}{H}}. \tag{5.15}$$

This leads immediately to

$$\frac{1}{\alpha_x} = 1 + H \quad \wedge \quad \frac{1}{\alpha_y} = 1 + \frac{1}{H} \tag{5.16}$$

through (5.13). These relations completely couple H, α_x and α_y so than only one needs to be measured to determine the others.

To couple the other scaling exponents, it is necessary to calculate another expression for $P(S)$. This is done via (5.12) and (5.15):

$$\begin{aligned} P(S)dS &= \int\limits_{S<f(l_x)<S+dS} P(l_x)dl_x \\ &\approx dS \int_{-\infty}^{\infty} \delta[S - f(l_x)]P(l_x)dl_x \\ \Rightarrow P(S) &= \int_{-\infty}^{\infty} \delta[S - f(l_x)]P(l_x)dl_x \\ &= \langle \delta[S - f(l_x)] \rangle. \end{aligned} \tag{5.17}$$

The derivation is identical for l_y, so

$$P(S) = \langle \delta[S - f(l_x)] \rangle = \langle \delta[S - g(l_y)] \rangle. \tag{5.18}$$

Performing the integration, the end result is

$$P(S) \sim S^{-\frac{\beta_x + H}{1+H}} \quad \wedge \quad P(S) \sim S^{-\frac{H\beta_y + 1}{1+H}}. \tag{5.19}$$

This gives the relation between the scaling exponents

$$\gamma = \frac{\beta_x + H}{1 + H} = \frac{\beta_y + \frac{1}{H}}{1 + \frac{1}{H}}. \tag{5.20}$$

Alternatively, γ can be eliminated so that

$$\beta_x = H\beta_y + 1 - H, \tag{5.21}$$

or H can be eliminated to result in

$$\beta_x = \frac{\gamma + \alpha_x - 1}{\alpha_x}, \tag{5.22}$$

which also applies for β_y and α_y.

The end result is that a minimum of only two of the exponents needs to be determined before all five are known. Measuring for instance α_x and β_x, the rest are given by (5.16) and (5.20)-(5.22).

In Figure 5.6, an attempt to extract β_x and β_y is shown. Due to the shape of the pinning clusters, there is only a very short data range available [17, 19]. Hence,

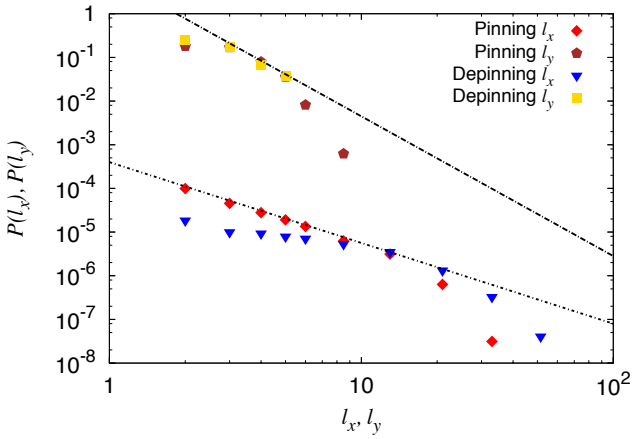

Figure 5.6: Probability distribution function of the linear extension of the clusters both parallel and perpendicular to the fracture front. The data for l_x are shifted for visual clarity by 10^{-3}. The slopes of the lines correspond to $\beta_x = 1.86$ and $\beta_y = 3.2$. Further details in the text.

the focus is to determine β_x as best as possible and verify that β_y is appropriate according to (5.21) and previously introduced measurements of H. In the figure, it is also visible for the depinning data how the finite size of the system suppresses the presence of the smallest cluster sizes because the available space is predominantly occupied by clusters of intermediate sizes. The extracted exponents are $\beta_x = 1.86 \pm 0.06$ (linear regression) and $\beta_y = 3.2$ [through (5.21)].

Examining $P(S)$, the data is plotted in Figure 5.7. A slope of $\gamma = 1.61$ seems to fit the numerical data. The value for γ is based on the derived scaling equations; the quality of the current data is unfortunately not sufficient to directly extract a value. This is discussed further in [17]. Only depinning data are included in the figure due to a more prominent cutoff in S for pinning clusters [17, 19]. The quality of the data is insufficient to determine in there is a difference in γ for depinning and pinning, but based on the experimental results [58], no such difference is expected.

A complete comparison between the scaling exponents measured experimentally, numerically and theoretically are given in Table 5.1. There is very good agreement between the different results. For the theoretical values, it is assumed $H = \zeta_{\text{small}}, \zeta_{\text{large}}$, and the reported γ-values are assumed to be correct. According to (5.16) and (5.20)-(5.22), in addition to H, either γ, β_x or β_y has to be known to calculate the other exponents. Since none of them can be determined in another manner, one of them was chosen according to measurements to allow a comparison between the other exponents. Note also that even though two values for H was found both numerically and experimentally, it seems that the distributions of S, l_x and l_y are controlled by the one which satisfies $H = \zeta$.

Table 5.1 is written such that it may seem that the theory claims that depinning

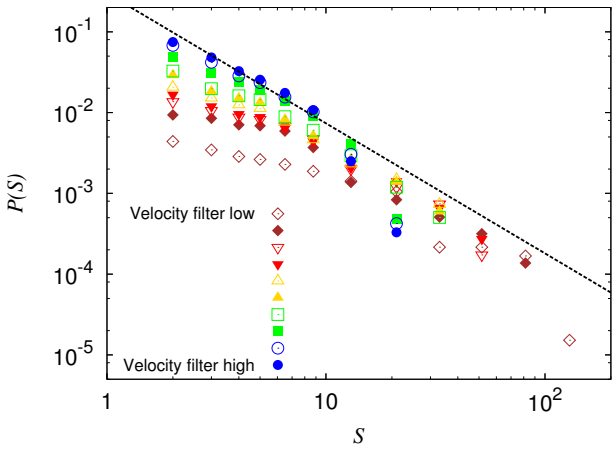

Figure 5.7: Size distribution of clusters. Only depinning data are included to present the suggested scaling as detailed as possible. Pinning clusters are inherently smaller and thus subjected to a cutoff at smaller S than depinning clusters. The slope of the line correspond to $\gamma = 1.61$. Further details in the text.

Table 5.1: Overview of scaling exponents gathered from both experiment [58] and simulations [17, 19], and comparison with theoretical predictions. Important notes on the theoretical values in the text. Numbers in parentheses indicate a high uncertainty.

		Experiment	Simulation	Theory
Depinning	H	0.66	0.67	$2/3$
	α_x	0.61	0.60	0.60
	α_y	0.41	0.40	0.40
	γ	1.56	(1.61)	1.56
	β_x	1.93	1.86	$1.9\overline{3}$
	β_y	2.36	(3.2)	2.40
Pinning	H	0.55	0.39	0.388
	α_x	0.63	0.76	0.72
	α_y	0.34	0.30	0.28
	γ	1.56	(1.61)	1.61
	β_x	1.93	(1.86)	1.86
	β_y	(2.36)	(3.2)	3.18

implies percolation type behaviour ($\zeta = 2/3$) and pinning implies elastic interactions ($\zeta = 0.388$). The situation is not that simple. It seems that both behaviours can be found in both pinning and depinning regimes, but that the probability distributions are controlled by whichever process that governs the roughness exponent. Whether γ is always controlled by the value of H which satisfies $H = \zeta$ and how the distribution functions behave in the transition $\zeta_{\text{small}} \to \zeta_{\text{large}}$ is uncertain.

Concerning local velocities

My impression is that the H based on the velocities closest to the average velocity gives the correct scaling. The more the velocity filter is applied, the more artificial behaviour is seen. In the paper [19], we reported also the result for $H_{\text{dep}}^{\text{high}}$. I believe this to be a trivial scaling resulting from the filtering process[4].

My hypothesis is that through (5.10), pinning is controlled by ζ_{large}, caused by the elastic interactions. Velocities with a high relative difference to $\langle v \rangle$ demonstrate a scaling similar to the depinning clusters, which are controlled by ζ_{small}, caused by random damage-percolation. The depinning clusters should behave the same for all velocities, but due to the size dependence, a trivial scaling is seen for the highest velocities [19]. This hypothesis could be strengthened or disproven through larger simulation data, unfortunately unavailable at the writing of this thesis. This should be investigated at a later date, but for the time being it is assumed that including the most velocity data gives the most correct scaling. This leads to a very good agreement between numerical simulations, experimental results, and theoretical predictions, as shown in Table 5.1.

It may seem natural to think that when the entire process is advanced by random selection of bonds, singular strong bonds could serve to pin and retard the fracture process. However, it is just the opposite. This individual pinning of bonds is more strongly felt in the fluctuating line regime as this information is transmitted across a large portion of the line through the elastic interactions. When the front is advanced through coalescence of damage, the random selection of weaker bonds further ahead can serve to accelerate the fracture process. Experimental evidence of this has recently been reported by Guerra et al. from a study in PMMA [23]. This is consistent with having a pinning regime described by ζ_{large} and a depinning regime described by ζ_{small}.

[4]Due to the limited system size, for a sufficiently high filter, little or no data is left. For a slightly smaller filter, the amount of clusters grow, but because of the resolution, they are "trivial" islands of 1×1, 2×1, 1×2, 2×2 and such; increasing in size for a decrease in velocity filter. This would give an apparent scaling of l_y as a function of l_x of close to unity. Coupled with a preference (due to stress conentration) of breaking lateral neighbouring bonds instead of penetrating deeper into the material, this could explain the observed scaling for high filter values in [19], where the value 0.9 was reported.

Chapter 6

Conclusion

> *Men fear death as dragons do not.*
>
> Orm Irian, *The other wind*, 1990

Together with my colleagues, I have developed a model to study in-plane fracture. The model is shown to contain two different fracture mechanisms leading to different behaviours of the fracture front.

Direct analysis of the fracture front yields two roughness regimes. One small scale regime characterised by

$$\zeta_{\text{small}} = \frac{2}{3},$$

as predicted from several models containing randomness alone [25, 29, 31, 32], and one large scale regime characterised by

$$\zeta_{\text{large}} = 0.39,$$

as predicted by the fluctuating line model [47].

Our model is very simple, containing in essence only a random selection process in conjunction with a correlation function based on linear elasticity theory. The fluctuating line behaviour is emergent from the correlation function and not an intentional construct in the model. This is an important distinguishing feature with our model compared to existing fluctuating line models, which are, to my knowledge, all based on direct modeling of equations derived from continuum mechanics.

Though the model is quasi-static, a study of the dynamics of the fracture processes has been performed. The results match those obtained experimentally [19, 58].

The agreement with experimental results leads me to conclude that our model gives a very accurate description of the physics involved. This implies that the roughness

exponent reported in the literature to be $\zeta \approx 0.55 - 0.63$ [13, 53] is an underestimation of the value $\zeta = 2/3$. My own results show that a lower value in this range seems to more prominent in a direct analysis of the front (Figure 4.4). However, the scaling relations derived theoretically yield values that match the experimental and numerical results when using $\zeta = 2/3$ as input, suggesting that if no other effects are present, one should expect a roughness exponent of exactly $2/3$.

The level of agreement in the measurements of H, both experimentally [58] and numerically [8, 19], suggests that one should be able to measure a value of ζ closer to $2/3$ if this theory is correct. However, the front roughness can be more sensitive to an unidentified cause than the local scaling which controls H, thus making ζ more difficult to pin down. This warrants further consideration.

Future work

There is one specific achievement I would have liked to accomplish during this work, and that is the simultaneous measurement of the two different roughness exponents in a single numerical simulation. Unfortunately, this requires a system size currently out of reach. Someone should consider writing a massively parallel piece of software and ask very politely to borrow large parts of K, Titan, or another supercomputer for a while.

Larger data sets should be simulated and the dynamics analysed to complete the analysis presented in section 5.2 and [17]. The data obtained so far are very promising. The current results paint a picture where there really are only two processes controlling the fracture, and suggests an interplay between local dynamics and more large scale front behaviour.

Other than that, the most interesting steps forward as I see it is to develop a full 3D model based on the same principles of our model and/or to include plasticity effects. A third suggestion, in some sense related to plasticity, is to change the shape and interaction of and between bonds. The current model uses essentially point interactions in the fracture process, and I would think it to be very interesting to try to use the same principles to model a, e.g., more fibrous material such as wood or paper. Glasses should also present an interesting challenge.

Recently, an experimental study showed fracture in PMMA through interesting micro-crack dynamics [23]. I am convinced our model can reproduce this behaviour, but this has not been investigated yet.

Final remarks

It is my hope that this work will lead to a deeper understanding of fracture phenomena, and I thank you for your attention.

Glossary

BLAS Basic Linear Algebra Subprograms, a numerical library of very efficient vector-vector, matrix-vector, and matrix-matrix operations (`www.netlib.org/blas`). 20, 51

brittle fracture A fracture process where the material breaks "abruptly", without or with very little deformation prior to destruction. Principal damage type is direct bond breaking. 2, 4, 5

CG Conjugate Gradient. 19, 20, 23

CPU Central Processing Unit. 20, 22, 27

cuBLAS nVidia's version of BLAS running on a compute capable graphics card, `https://developer.nvidia.com/cublas`. 20

CUDA Compute Unified Device Architecture, an extension to standard C, it allows for general purpose computing on the graphics card (GPU). Closed source (nVidia), OpenCL is an open source alternative. 20

cuFFT nVidia's library to do Fourier transform, essentially FFTW on the graphics card, `https://developer.nvidia.com/cufft`. 20

dense A property of a matrix indicating that is mostly (or completely) contains non-zero elements, as opposed to: sparse. 19, 54

disorder see: quenched disorder. 14

ductile fracture A fracture process where the material undergoes plastic deformations, stretching, prior to destruction. Damage can be through void formation and growth, often associated with structural dislocations. 4, 5

dynamic exponent An exponent characterising dynamical processes, for instance the dependence on the correlation length ξ of the characteristic time in a system, $t \sim \xi^z$. See also: Family-Vicsek scaling. 38, 39

ELS equal load sharing. 19, 39

EPFM elasto-plastic fracture mechanics. 3, 23

Family-Vicsek scaling If something grows with a width as a function of global size and time so that $w(L,t) \sim t^b$ up to a certain time t^* and $w(L,t) \sim L^\zeta$ afterwards, Family and Vicsek had the idea that $t^* \sim L^z$. This means that $z = \zeta/b$ and the overall growth can be described as $w(L,t) \sim L^\zeta f(t/L^z)$. This is the Family-Vicsek scaling relation. The scaling function has the properties $f(x) = x^b (x \ll 1), 1 (x \gg 1)$. 34, 38, 51, 52, 54

FFTW Fastest Fourier Transform in the West, a very efficient numerical library to do Fourier transforms (`www.fftw.org`). 20, 51

fluctuating line model Any model where main concept is to study the movement of an elastic line being pulled through a disordered medium (my definition). 10–12

foreign function interface or FFI, is a collection of methods/functions in one programming language written specifically to call methods/functions written in another language. Typically used to access library functions written in language different from the language used for control structures, for example numerical or graphical libraries. 20

Fourier space The frequency space the transformed function is in as a result of a Fourier transform. 16

Fourier transform A mathematical transform which turns a function of time into a function of frequency through the integral $F(x) = \int_{-\infty}^{\infty} f(t) e^{-2\pi i x t} dt$. 16, 20, 51, 52

FPZ fracture process zone. 3

fractal dimension A measure of fractality, see explanation on page 6, section 1.2. 5–7, 9

GPU Graphics Processing Unit. 20–22, 27, 51

Green's function A Green's function is a type of function used to solve inhomogeneous differential equations. In physics, the term is often used to refer to various types of correlation functions. 14–18, 20, 23, 26, 27, 29, 39, 63

growth exponent An exponent describing (typically) initial dependence on time for some process. In the context of fracture fronts, it governs how the width of the front widens or roughens with time, $w \sim t^b$. See also: Family-Vicsek scaling. 38

Hooke's law Hooke's law states that the applied force is proportional to the achieved extension. Typical example system: a spring, $f = kx$. 14

interstitial Something forming or occupying interstices ([very] small intervening space). Typically refers to (in this setting) in-plane fracture where the weak

plane can be considered an intervening space between two solids. 10

iterativeness A property of an object which is created or where parts of the structure is created by a repeated process. 5

K Currently the most powerful computer in Japan (`http://www.aics.riken.jp/en/`). 50

LEFM linear elastic fracture mechanics. 2–4, 14, 23

linear algebra Field in mathematics concerned with solving linear equations and sets of linear equations, that is equations on the form $a_1x_1 + a_2x_2 + \cdots = b$. 15

maximum norm The maximum norm is the infinite p-norm on a compact set U. For a vector of finite dimensions, $||x||_\infty = \max(|x_1|, \ldots, |x_n|)$. 23

MD molecular dynamics. 3

Monte Carlo process A process using a statistical sample of configurations of a system chosen on the basis of randomly generated numbers to study (often complex) properties of the said system. In this context, a way to randomly sample independent configurations of a system. 21

morphology Having to do with the change in physical appearance. i, 1, 9, 21

multi-affine Connected to self-affinity, if the height-height correlation function $c_q(x,a)^{1/q} = \langle|h(x+a)-h(x)|^q\rangle^{1/q}$ is independent of q, the function in question is self-affine. If, on the other hand, $c_q(x,a)^{1/q}$ changes with q, the function is multi-affine. 11, 12

NLEFM non-linear elastic fracture mechanics. 2, 3, 23

nowhere differentiable A property of a function whose derivative does not exist at any point. 6

percolation per-colare (lit.) means "through-to strain". Percolation theory describes the behaviour of connected clusters or domains in a random graph. If A and B are two points on a random graph, they are connected if something can percolate between them. i, 10–12, 18, 26, 31, 33–35, 39, 41, 47, 48

Poisson ratio When something is stretched/squeezed to an extension/contraction in the direction of applied load, the material responds with a contraction/extension in the direction perpendicular to the applied load. The ratio between the strains is the Poisson ratio. 14

positive definite A property of a matrix $\mathbb{A}$ meaning that for any non-zero vectors x, the product $x^{\mathrm{T}}\mathbb{A}x$ is always positive. Positive semi-definiteness means that $x^{\mathrm{T}}\mathbb{A}x \geq 0$. 15–17, 19

quasistatic A quasistatic process is a process that happens infinitely slowly. It is a dynamic process (something happens), but dynamics in the process are neglected (allowing infinite speeds, no inertial effects, et c.). 16, 37

quenched disorder Disorder in physics usually means the addition of something random to an ordered system. Quenched means that this randomness is static and already in place since the beginning, as opposed evolving in any way with time. 14, 25, 51

random graph A mathematical representation of a set of objects connected in some form through links generated by some random process. 53

roughness exponent A number detailing how the width of a general interface (here: interface between broken and unbroken material, fracture fronts) changes with the perceived length of the interface, $w \sim l^{\zeta}$. $w \times l$ are the dimensions of a box that would enclose the entire interface. See also: Family-Vicsek scaling. i, 10–12, 26, 39, 41–43, 48–50

SBCL Steel Bank Common Lisp. 20

self-affine See explanation on page 7, section 1.2. 7, 9–12, 31, 53

self-similar See explanation on page 6, section 1.2. 5–7, 9, 11, 31

SOS Solid-on-solid, a way to remove multiple values in a function by (usually) selecting either the highest or lowest value. The name comes from the approximation that a complex interface is collapsed down to the line representing the first change from region A to region B as looked from above or below. Two solids meeting, not mixing liquids. 11, 30, 31

sparse A property of a matrix indicating that is mostly (or completely) contains zeroes, as opposed to: dense. 19, 51

strain The relative change in elongation of a sample under load. 2, 3, 16, 22, 29

stress Pressure or tension acting on an object. i, 2, 3, 22, 25, 26, 29

stress-intensity factor A number detailing the stress rate near the crack front or tip. Used in fracture mechanics and materials testing to predict material toughness; a sample can undergo fracture when $K_{\text{measured}} > K_{\text{crit-theory}}$. 2, 25

symmetric There are many forms of symmetries. In the context of a symmetric matrix $\mathbb{A}$, its elements obey $a_{ij} = a_{ji}$. 17

tension One of the three modes of loading, tension is often referred to as opening stress and can be described as loading parallel to the principal axis of a sample. 16

Titan Currently the most powerful computer in the world, as of November 2012 (`http://www.olcf.ornl.gov/titan/`). 50

trace The trace of an $n \times n$ real matrix is the sum of all diagonal elements, $\mathrm{tr}(A) = \sum_{i=1}^{n} a_{ii}$. 16

translational invariant A property of any function that obeys $f(x) = f(x + t)$ for any arbitrary translation t and coordinate x. 16

WTM waiting time matrix. 41

Young's modulus Also called tensile stress, it is a material constant and a measure of the ratio of stress to strain for a material. 2, 14, 26, 43

References

[1] Mikko J Alava, Phani Kumar V V Nukala, and Stefano Zapperi. Statistical models of fracture. *Advances in Physics*, 55(3-4):349–476, May 2006.

[2] Mikko J Alava and Stefano Zapperi. Comment on: "Roughness of Interfacial Crack Fronts: Stress-Weighted Percolation in the Damage Zone". *arXiv:cond-mat/0401568v1*, 2004.

[3] Ted L Anderson. *Fracture Mechanics*. CRC Press, 3rd edition, 2005.

[4] Albert-László Barabási and H Eugene Stanley. *Fractal Concepts in Surface Growth*. Camebridge University Press, 1995.

[5] Ghassan George Batrouni, Alex Hansen, and Jean Schmittbuhl. Heterogeneous interfacial failure between two elastic blocks. *Physical Review E*, 65(3):036126, February 2002.

[6] Daniel Bonamy. Intermittency and roughening in the failure of brittle heterogeneous materials. *Journal of Physics D: Applied Physics*, 42(21):214014, November 2009.

[7] Daniel Bonamy and Elisabeth Bouchaud. Failure of heterogeneous materials: A dynamic phase transition? *Physics Reports*, 498(1):1–44, 2011.

[8] Daniel Bonamy, Stéphane Santucci, and Laurent Ponson. Crackling Dynamics in Material Failure as the Signature of a Self-Organized Dynamic Phase Transition. *Physical Review Letters*, 101(4):045501, July 2008.

[9] Elisabeth Bouchaud, G Lapasset, and J Planès. Fractal Dimension of Fractured Surfaces: A Universal Value? *Europhysics Letters*, 13(1):73–79, 1990.

[10] J P Bouchaud, Elisabeth Bouchaud, G Lapasset, and J Planès. Models of fractal cracks. *Physical Review Letters*, 71(14):2240–2244, 1993.

[11] Eugene Butkov. *Mathematical physics*. Addison-Wesley, World student series, 1973.

[12] Antoine de Saint-Exupéry. *Le Petit Prince*. Éditions Gallimard, 1943.

[13] Arnaud Delaplace, Jean Schmittbuhl, and Knut Jørgen Måløy. High resolution description of a crack front in a heterogeneous Plexiglas block. *Physical Review E*, 60(2):1337–43, August 1999.

[14] Fereydoon Family and Tamás Vicsek. Scaling of the active zone in the Eden process on percolation networks and the ballistic deposition model. *J. Phys. A: Math. Gen.*, 18:75–81, 1985.

[15] Jens Feder. *Fractals*. Plenum Press, New York, 1988.

[16] Knut Skogstrand Gjerden. Making the case of GPUs in courses on computational physics. *Submitted to EJP*, 2012.

[17] Knut Skogstrand Gjerden. On the universality classes found in interfacial brittle fracture. *In preparation*, 2013.

[18] Knut Skogstrand Gjerden, Arne Stormo, and Alex Hansen. A model for stable interfacial crack growth. *Journal of Physics: Conference Series*, 402:012039, 2012.

[19] Knut Skogstrand Gjerden, Arne Stormo, and Alex Hansen. Local dynamics of a randomly pinned crack front: A numerical study. *In preparation*, 2013.

[20] Knut Skogstrand Gjerden, Arne Stormo, and Alex Hansen. Universality Classes in Constrained Crack Growth. *arXiv:1301.2174 (Submitted to PRL)*, 2013.

[21] Jean-François Gouyet and Michel Rosso. Diffusion fronts and gradient percolation: A survey. *Physica A: Statistical Mechanics and its Applications*, 357(1):86–96, November 2005.

[22] A A Griffith. The Phenomena of Rupture and Flow in Solids. *Philosophical Transactions A*, 221:163–198, 1920.

[23] Claudia Guerra, Julien Scheibert, Daniel Bonamy, and Davy Dalmas. Understanding fast macroscale fracture from microcrack post mortem patterns. *Proceedings of the National Academy of Sciences USA*, 109(2):390, 2012.

[24] Jan Øystein Haavig Bakke and Alex Hansen. Accuracy of roughness exponent measurement methods. *Physical Review E*, 76(3):031136, September 2007.

[25] Alex Hansen, Ghassan George Batrouni, Thomas Ramstad, and Jean Schmittbuhl. Self-affinity in the gradient percolation problem. *Physical Review E*, 75(3):030102, March 2007.

[26] Alex Hansen and Joachim Mathiesen. Survey of Scaling Surfaces. In *Modelling Critical and Catastrophic Phenomena in Geoscience*, chapter 5, pages 93–110. Springer, New York, 2006.

[27] Alex Hansen and Stéphane Roux. Statistics toolbox for damage and fracture. In *Damage and Fracture of Disordered Materials*, chapter 2, pages 17–101. Springer, New York, 2000.

[28] Alex Hansen, Jean Schmittbuhl, and Ghassan George Batrouni. Distinguishing fractional and white noise in one and two dimensions. *Physical Review E*, 63(6):062102, May 2001.

[29] David A Huse and Christopher L Henley. Pinning and roughening of domain walls in Ising systems due to random impurities. *Physical Review Letters*, 54(25):2708–2711, 1985.

[30] G R Irwin. Analysis of Stresses and Strains near the End of a Crack Traversing a Plate. *Journal of Applied Mechanics*, 24:109–114, 1957.

[31] Mehran Kardar. Roughening by impurities at finite temperatures. *Physical Review Letters*, 55(26):2923, 1985.

[32] Mehran Kardar and David R Nelson. Commensurate-incommensurate transitions with quenched random impurities. *Physical Review Letters*, 55(11):1157, 1985.

[33] Alejandro B Kolton, Alberto Rosso, and Thierry Giamarchi. Creep Motion of an Elastic String in a Random Potential. *Physical Review Letters*, 94(4):047002, February 2005.

[34] Alejandro B Kolton, Alberto Rosso, Thierry Giamarchi, and Werner Krauth. Dynamics below the Depinning Threshold in Disordered Elastic Systems. *Physical Review Letters*, 97:057001, 2006.

[35] A I Larkin and Yu N Ovchinnikov. Pinning in type II superconductors. *Journal of Low Temperature Physics*, 34(3-4):409–428, February 1979.

[36] Lasse Laurson, Stéphane Santucci, and Stefano Zapperi. Avalanches and clusters in planar crack front propagation. *Physical Review E*, 81:046116, April 2010.

[37] A E H Love. The Stress Produced in a Semi-Infinite Solid by Pressure on Part of the Boundary. *Philosophical Transactions of the Royal Society A: Mathematical, Physical and Engineering Sciences*, 228(659-669):377–420, January 1929.

[38] Knut Jørgen Måløy, Stéphane Santucci, Jean Schmittbuhl, and Renaud Toussaint. Local Waiting Time Fluctuations along a Randomly Pinned Crack Front. *Physical Review Letters*, 96(4):045501, January 2006.

[39] Knut Jørgen Måløy and Jean Schmittbuhl. Dynamical Event during Slow Crack Propagation. *Physical Review Letters*, 87(10):105502, August 2001.

[40] Knut Jørgen Måløy, Jean Schmittbuhl, Alex Hansen, and Ghassan George Batrouni. Scaling and dynamics of an interfacial crack front. *International Journal of Fracture*, 121:9–22, 2003.

[41] Benoit B Mandelbrot. How long is the coast of britain? Statistical self-similarity and fractional dimension. *Science*, 156(3775):636–638, May 1967.

[42] Benoit B Mandelbrot, Dann E Passoja, and Alvin J Paullay. Fractal character of fracture surfaces of metals. *Nature*, 308(5961):721–722, 1984.

[43] Ali Reza Mehrabi, Hossein Rassamdana, and Muhammad Sahimi. Characterization of long-range correlations in complex distributions and profiles. *Physical Review E*, 56(1):712–722, 1997.

[44] Sylvain Patinet, Daniel Bonamy, and L Proville. Atomic-scale avalanche along a dislocation in a random alloy. *Physical Review B*, 84(17):174101, November 2011.

[45] Laurent Ponson and Daniel Bonamy. Crack propagation in brittle heterogeneous solids: Material disorder and crack dynamics. *International Journal of Fracture*, 162(1-2):21–31, April 2010.

[46] J R Rice. A Path Independent Integral and the Approximate Analysis of Strain Concentration by Notches and Cracks. *Journal of Applied Mechanics*, 35:379–386, 1968.

[47] Alberto Rosso and Werner Krauth. Roughness at the depinning threshold for a long-range elastic string. *Physical Review E*, 65(2):025101, January 2002.

[48] Stéphane Santucci, M Grob, Renaud Toussaint, Jean Schmittbuhl, Alex Hansen, and Knut Jørgen Måløy. Fracture roughness scaling: A case study on planar cracks. *Europhysics Letters*, 92(4):44001, November 2010.

[49] Stéphane Santucci, Knut Jørgen Måløy, Arnaud Delaplace, Joachim Mathiesen, Alex Hansen, Jan Øystein Haavig Bakke, Jean Schmittbuhl, Loïc Vanel, and Purusattam Ray. Statistics of fracture surfaces. *Physical Review E*, 75(1):016104, January 2007.

[50] B Sapoval, Michel Rosso, and Jean-François Gouyet. The The fractal nature of a diffusion front and the relation to percolation. *J. Physique Lett.*, 46(4):L149–L156, 1985.

[51] Jean Schmittbuhl, Arnaud Delaplace, and Knut Jørgen Måløy. Propagation of an interfacial crack front in a heterogeneous medium: Experimental observations. In *Physical Aspects of Fracture*, pages 353–369. Kluwer Academic Publishers, 2001.

[52] Jean Schmittbuhl, Alex Hansen, and Ghassan George Batrouni. Roughness of Interfacial Crack Fronts: Stress-Weighted Percolation in the Damage Zone. *Physical Review Letters*, 90(4):045505, January 2003.

[53] Jean Schmittbuhl and Knut Jørgen Måløy. Direct Observation of a Self-Affine Crack Propagation. *Physical Review Letters*, 78(20):3888, 1997.

[54] Jean Schmittbuhl, Stéphane Roux, Jean-Pierre Vilotte, and Knut Jørgen Måløy. Interfacial Crack Pinning: Effect of Nonlocal Interactions. *Physical Review Letters*, 74(10):1787–1790, September 1995.

[55] Bruce Short. Imhotep and the Origins of Ancient Egyptian Military Medicine. *ADF Health*, 10(1):48–50, 2009.

[56] Ingve Simonsen, Alex Hansen, and Olav Nes. Determination of the Hurst exponent by use of wavelet transforms. *Physical Review E*, 58(3):2779–2787, September 1998.

[57] Arne Stormo, Knut Skogstrand Gjerden, and Alex Hansen. Onset of localization in heterogeneous interfacial failure. *Physical Review E*, 86:025101, August 2012.

[58] Ken Tore Tallakstad, Renaud Toussaint, Stéphane Santucci, Jean Schmittbuhl, and Knut Jørgen Måløy. Local dynamics of a randomly pinned crack front during creep and forced propagation: An experimental study. *Physical Review E*, 83(4):046108, April 2011.

[59] Anne Tanguy and T Vettorel. From weak to strong pinning I: A finite size study. *European Physical Journal B*, 38:71–82, 2004.

[60] Peter Thompson. How Much Did the Liberty Shipbuilders Learn? New Evidence for an Old Case Study. *Journal of Political Economy*, 109(1):103–137, 2001.

[61] H M Westergaard. Bearing Pressures and Cracks. *Journal of Applied Mechanics*, 6:49–53, 1939.

A model for stable interfacial crack growth

Journal of Physics: Conference Series, **402**:012039 (2012)

Paper I

Erratum:

An error has unfortunately been included in the published version of this paper. In the explicit equation for u_i, (6) on page 4, there is missing a factor 1/4 in the pre-factor and the sentence directly above should read "(...) acting on the area $4a^2$ at the origin as ". The original derivation by [37] was performed on a rectangle of size $2a \times 2b$. This area should not be confused with the Green's function on integral form, (3b) on page 2, where the integration is carried out over the area a^2. The a in (6) was renamed in later versions of this paper to avoid any confusion, but the original naming unfortunately made it into the published version.

A model for stable interfacial crack growth

Knut S Gjerden[1], Arne Stormo[1], Alex Hansen[1]

[1] Department of Physics, Norwegian University of Science and Technology, N-7491 Trondheim, Norway

E-mail:
knut.skogstrand.gjerden@gmail.com,arne.stormo@gmail.com,Alex.Hansen@ntnu.no

Abstract. We present a model for stable crack growth in a constrained geometry. The morphology of such cracks show scaling properties consistent with self affinity. Recent experiments show that there are two distinct self-affine regimes, one on small scales whereas the other at large scales. It is believed that two different physical mechanisms are responsible for this. The model we introduce aims to investigate the two mechanisms in a single system. We do find two distinct scaling regimes in the model.

Is not included due to copyright

Onset of localization in heterogeneous interfacial failure

Physical Review E **86**, 025101(R) (2012)

Paper II

PHYSICAL REVIEW E **86**, 025101(R) (2012)

Onset of localization in heterogeneous interfacial failure

Arne Stormo,[*] Knut Skogstrand Gjerden,[†] and Alex Hansen[‡]
Department of Physics, Norwegian University of Science and Technology, N-7491 Trondheim, Norway
(Received 15 February 2012; published 10 August 2012)

We study numerically the failure of an interface joining two elastic materials under load using a fiber bundle model connected to an elastic half space. We find that the breakdown process follows the equal load sharing fiber bundle model without any detectable spatial correlations between the positions of the failing fibers until localization sets in. Depending on the elastic constant describing the elastic half space, localization sets in before or after the critical load causing the interface to fail completely is reached. There is a crossover between failure due to localization and failure without spatial correlations when tuning the elastic constant, not a phase transition as has been proposed earlier. Also, contrary to earlier claims based on models different from ours, we find that a finite fraction of fibers must fail before the critical load is attained, even in the extreme localization regime, i.e., for very small elastic constant. We furthermore find that the critical load remains finite for all values of the elastic constant in the limit of an infinitely large system.

DOI: 10.1103/PhysRevE.86.025101 PACS number(s): 81.40.Pq, 81.40.Np, 62.20.mm, 83.80.Ab

The joining of interfaces, e.g., by welding or gluing, is an important part of everyday technology; a technology that has been refined through the centuries. When joined interfaces are subject to excessive loads, failure occurs. Often it is not the joints themselves that fail, but the material that surrounds them, as the joints themselves are the stronger.

The aim of this work is, however, not to study failure of such joints with improvement of technology in mind. Rather, we take the point of view that failure of a heterogeneous joined interface provides a simplified model for fracture in bulk materials. Such an idea is not new. Schmittbuhl *et al*. [1] and Schmittbuhl and Måløy [2] studied, first computationally, then experimentally, the roughness of the fracture front moving through a sintered interface between two Plexiglas plates that are being plied apart in a mode-I fashion. The study of the fluctuations of this fracture front provides much insight into the much more complex morphology of three-dimensional fracture surfaces [3].

We focus on the phenomenon of *localization* in this work. Local failure occurs either because the material is weaker at that spot or because it is more loaded there than elsewhere. Differences in local strength is due to heterogeneities. Differences in loading is due to structure in the stress field. If we assume that the interface is loaded uniformly, the local stress field will be quite uniform. Local failure will occur because of material weakness. For the simple reason that the farther away we search from a point where a failure has occurred, the weaker the weakest spot we have found so far will be, localization is disfavored. Heterogeneity in strength induces a "repulsion" between the local failures. However, when failed areas build up, local stress is concentrated at the rim of the failed areas making these regions liable to fail. Heterogeneity in the stress field induces an "attraction" between local failures.

Localization occurs when attraction wins over repulsion. A transition in the failure process occurs at this point. What is the nature of this transition? A number of papers have addressed this question in the context of fracture. Zapperi *et al*. [4] studied the *fuse model* and concluded that the breakdown process is a driven first-order transition in this system. The mechanism behind this phase transition is the accumulation of damage as the fracture process proceeds. Garcimartin *et al*. [5] studied experimentally mode-I fracture monitoring acoustic emission, thereby being able to visualize the fracture process. They concluded that the fracture process is a second-order phase transition. Using a local-load sharing fiber bundle model with thermally activated failures, Yoshioka *et al*. [6] concluded that the onset of localization is a second-order phase transition, related to the percolation transition.

In the model we study here, we find a third type of behavior. Localization and hence catastrophic failure in our system is neither a first- nor a second-order phase transition, but a *crossover* phenomenon.

When localization sets in immediately in the breakdown process, it is normally expected that the system is infinitely fragile in the limit of infinitely large system: As soon as a single fiber breaks at a given load, the entire system breaks down at that load [7]. As we will demonstrate, this is *not* the case here.

We base our work on the discretized model for interfacial failure proposed by Batrouni *et al*. [8]. A square array of $L \times L = N$ linearly elastic fibers placed a distance a apart connects a stiff half space with a linearly elastic half space characterized by Young's modulus E and a Poisson ratio ν (for which we assume a typical value of 0.25 in the following). Each fiber, indexed by i, has an elastic constant k and fails irreversibly if it is elongated beyond an individual threshold value t_i. The threshold values are drawn from a uniform distribution on the unit interval.

The separation of the two half spaces are controlled by displacing the hard medium by a distance D orthogonal to the interface where the fibers sit. Fiber i then experiences a force

$$f_i = -k(u_i - D), \tag{1}$$

[*]arne.stormo@gmail.com
[†]knut.skogstrand.gjerden@gmail.com
[‡]Alex.Hansen@ntnu.no

where u_i is the local displacement of the softer half space at the position of fiber i. The forces from the fibers are transmitted through the softer elastic medium via Green's function [9–11]

$$u_i = \sum_j^N G_{ij} f_i, \tag{2}$$

where

$$G_{ij} = \frac{1-\nu^2}{\pi E a^2} \iint_{-a/2}^{a/2} \frac{dx'dy'}{|\vec{r}_i(x,y) - \vec{r}_j(x',y')|}. \tag{3}$$

$\vec{r}_i - \vec{r}_j$ denotes the distance between fibers i and j at positions $\vec{r}_i$ and $\vec{r}_j$, respectively.

Green's function (3) is modified by the presence of boundaries due to the finite size $(La) \times (La) = Na^2$ of the interface. We assume periodic boundary conditions and take into account the first reflected images.

We note that if distances are measured in units of a, Green's function (3) is proportional to $(Ea)^{-1}$. Likewise, from Eq. (1), we see that the elastic constant of the fibers k must be proportional to a^2. Hence, if we change the linear size of the system, $(La) \to \lambda(La)$, while keeping the discretization a fixed, we change only $L \to \lambda L$ in the model whereas we keep the parameters Ea and k fixed. On the other hand, if we change the discretization $a \to a/\lambda$ while leaving the size of the system fixed, we change $L \to \lambda L$ and the parameters $(Ea) \to (Ea)\lambda$ and $k \to k/\lambda^2$.

A given fiber breaks irreversibly (its elastic constant is set to zero) if stretched beyond a threshold value assigned from a spatially uncorrelated probability distribution. We choose the simplest: a uniform distribution. The model is quasistatic, and in lieu of time, we measure the fraction of fibers that have broken, denoted by p. The load carried by the system is $\sigma(p) = \sum_i^N f_i/N$, and when σ reaches its maximum, any extra load will result in a complete catastrophic failure. We denote this the *critical load*, σ_c, and the corresponding p_c, the *failure point*.

In the limit of $(Ea/L) \to \infty$, the model becomes identical to the equal load sharing (ELS) fiber bundle model [7,12,13]. On the other hand, for small values of (Ea/L), it does not approach any existing models. Models do exist, e.g., the local load sharing (LLS) fiber bundle model [14], where the nearest surviving fibers absorb the entire load that a fiber was carrying when failing. Another model, introduced by Hidalgo *et al.* [15], distributes the added load around a failed fiber as a power law in the distance from the failed fiber. In both models, there is no elastic response by the planes defining the interface.

We have studied systems of size $L = 256$, $L = 128$, $L = 64$, $L = 32$, $L = 16$, and $L = 8$ with 10, 100, 1000, 10 000, 10 000, and 10 000 samples, respectively. We explore a range of elastic constants $e \equiv (Ea/L)$ in the range $e_{\text{soft}} \leqslant e \leqslant e_{\text{stiff}}$, where $e_{\text{soft}} = 2^{-17} = 7.63 \times 10^{-6}$ and $e_{\text{stiff}} = 2^6 = 32$.

To visualize localization, we record the square distance between consecutively failing fibers, Δr^2. If the positions of the failing fibers are completely random, as is the case in the ELS fiber bundle model, the average distance is $\langle \Delta r^2 \rangle^{1/2} = L/\sqrt{6} \approx 0.408L$. We show in Figure 1 a succession of histograms of $(\Delta r^2)^{1/2}$. That is, we record $\Delta r^2(n)$ as a function of the number of failed fibers, $n = pN$, our "time" parameter. We then sum the number of times $\Delta r(n)$ has had a particular

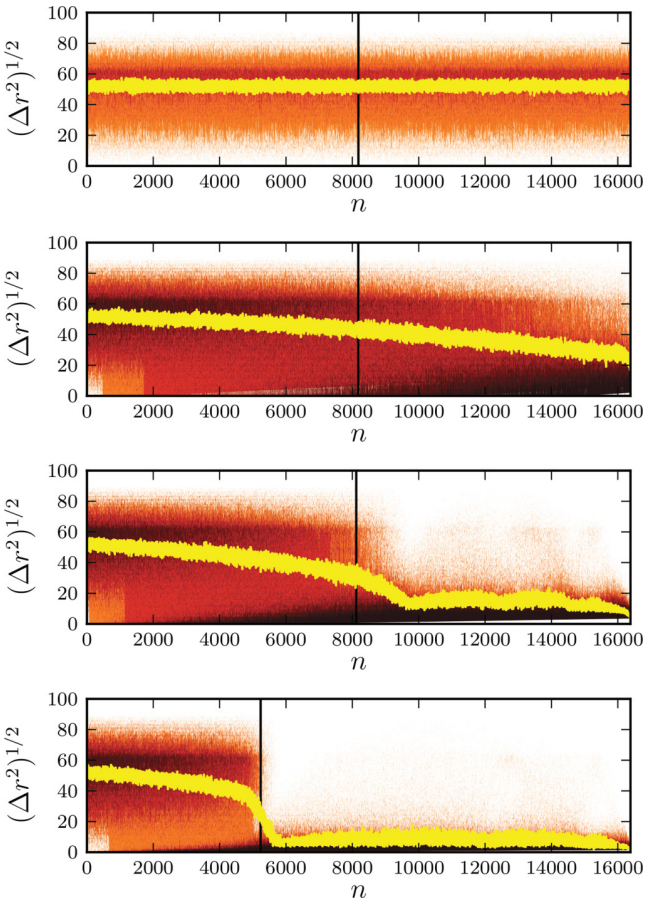

FIG. 1. (Color online) Histogram over the distance between consecutively failing fibers, $(\Delta r^2(n))^{1/2}$, as function of the number of failed fibers $n = pN$. Darker colors correspond to higher density. The vertical bar indicates the failure point, $p_c N$. The curve shows the running average $\langle \Delta r^2(n) \rangle^{1/2}$. In all figures, $L = 128$. 100 simulations was used to construct the histogram. From top to bottom, $e = 32$, $e = 2^{-3.678} = 0.0781$, $e = 2^{-6} = 0.0156$ and $e = 2^{-17} = 7.63 \cdot 10^{-6}$.

value $(\Delta r^2)^{1/2}$ at n for several independent simulations, hence creating a histogram for each n. Darker colors signifies more hits at that value of $(\Delta r)^{1/2}$. The curve shows the average value $\langle \Delta r^2(n) \rangle^{1/2}$ plotted against n. With $L = 128$, we see that for the four different elastic constants e that we show, $e = 32$, $e = 2^{-3.678}$ (this value is chosen to make the figure comparable to the results in Batrouni *et al.* [8], where $L = 128$, $E = 10$, and $a = 1$, which gives $e = 0.0781 = 2^{-3.678}$), $e = 2^{-6}$, and $e = 2^{-17}$, $\langle \Delta r^2(n) \rangle^{1/2}$ starts out being close to the ELS fiber bundle model value 52.26. The vertical bar in each figure shows the failure point $n_c = p_c N$.

Raising the value of the elastic constant e above e_{stiff} or below e_{soft} will not lead to changes from the uppermost and lowermost panels in Figure 1. At the highest value of e, the system behaves as the ELS fiber bundle model throughout the entire breakdown process: The average distance between consecutively failing fibers, $\langle \Delta r^2(n) \rangle^{1/2}$, remains constant throughout the process. The ELS fiber bundle model predicts $p_c = 1/2$ so that $n_c = 8192$.

As the system gets softer, both $\langle \Delta r^2(n) \rangle^{1/2}$ and n_c decrease. We see in the three lower panels in Figure 1 that there is an

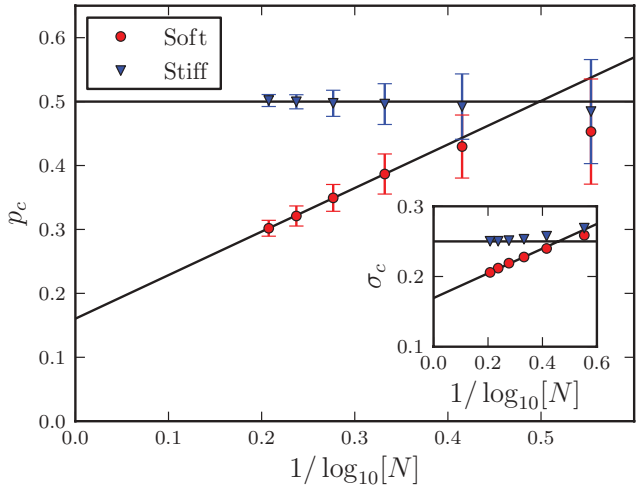

FIG. 2. (Color online) Finite-size analysis of failure point and critical loading. Both p_c (main plot) and σ_c (encapsulated) are plotted against $1/\log_{10}[N]$ for $N = 8^2 = 256$ to $N = 256^2 = 65536$ and both have finite values for any N. The slope of the soft systems are $\alpha_{p_c} = 0.68$ and $\alpha_{\sigma_c} = 0.16$.

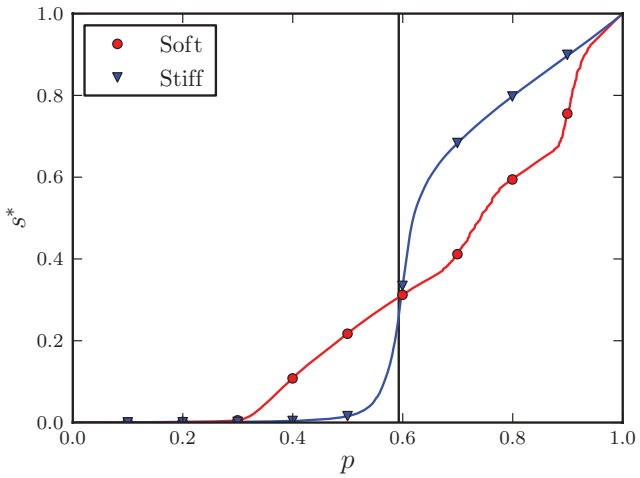

FIG. 3. (Color online) Density of the largest cluster of failed fibers, s^*, as a function of the damage p for $e = e_{\text{stiff}}$ and $e = e_{\text{soft}}$. Here $L = 128$. The vertical bar indicates the percolation point $p = 0.59274$.

abrupt change in $\langle \Delta r^2(n) \rangle^{1/2}$ for some range of n values. This is localization. We also see that the failure point does *not* fall to zero as e is lowered. Even for the smallest value in Figure 1, $e = e_{\text{soft}} = 2^{-17}$, n_c is significantly different from zero.

Figure 2 shows the failure point p_c as a function of the inverse of the logarithm of total number of fibers, $1/\log_{10}[N]$. From this figure, we may extrapolate the value of p_c in the limit of an infinitely large system. We find $\lim_{N\to\infty} p_c(N) \equiv p_c^\infty = 0.16$ when $e = e_{\text{soft}}$ and $p_c^\infty = 0.5$ when $e = e_{\text{stiff}}$. Likewise, we may extrapolate the critical load σ_c; see the insert in the figure. We find through extrapolation that $\sigma_c^\infty = 0.17$ for $e = e_{\text{soft}}$ and $\sigma_c^\infty = 0.25$ for $e = e_{\text{stiff}}$, the value expected for the ELS fiber bundle model.

It is a surprising result that neither p_c^∞ nor σ_c^∞ are zero for small value of e. The LLS fiber bundle model predicts that $\sigma_c \sim 1/\log_{10}[N]$ with $\sigma_c^\infty = 0$ [16,17]. Hidalgo *et al.* [15] present numerical evidence that their model also has $\sigma_c^\infty = 0$. Hence, in both of these models, $p_c^\infty = 0$.

Batrouni *et al.* [8] studied the structure of the clusters of failed fibers at p_c, claiming that at the failure point, they are distributed according to a power law with exponent -1.6. This would indicate a critical point at $p = p_c$.

Referring to Figure 1, we see that for $e = e_{\text{stiff}} = 32$, the system behaves as the ELS fiber bundle model where the position of the fibers that fail bear no correlations among themselves. This is clear from observing the average distance between consecutively failing fibers, $\langle \Delta r(n)^2 \rangle^{1/2}$, which essentially remains close to the ELS fiber bundle, where $\langle \Delta r^2(n) \rangle^{1/2} = L/\sqrt{6}$. Hence, we expect that the clusters follow *percolation* theory [18]. In Figure 3 we show the density of the largest cluster of failed fibers, s^*, as a function of p for $e = e_{\text{stiff}}$ and $e = e_{\text{soft}}$. In the case of the soft system, we see that at $p \approx 0.25$, the largest cluster becomes visible and grows essentially linearly with p. This behavior is due to localization. When p approaches 1, there are jumps in s^*, because of coalescence of clusters. On the other hand, when $e = e_{\text{stiff}}$, we see behavior consistent with percolation theory. When p is in the vicinity of $p = 0.59274$, the site percolation threshold on the square lattice [19], s^* shoots up and thereafter evolves linearly in p.

The failure point at which the system fails catastrophically, p_c, occurs long before the jump in s^* for $e = e_{\text{stiff}}$. This is an indication that the system is *not* critical at the failure point. Schmittbuhl *et al.* [20] measured the fluctuations of the failure point as a function of the system size, finding $\Delta p_c \sim 1/L^{0.65}$. This is consistent with the ELS fiber bundle model. Daniels and Skyrme [21] showed that the statistical distribution of the critical elongation in the ELS fiber bundle model has has the form

$$\rho(u_c)du_c = N^{1/3} f[CN^{1/3}(u_c - \langle u_c \rangle)]du_c, \tag{4}$$

where C is a constant only dependent on the threshold distribution and u_c is the critical elongation. This leads immediately to

$$\Delta p_c \sim \langle (u_c - \langle u_c \rangle)^2 \rangle^{1/2} \sim N^{-1/3} = L^{-2/3}, \tag{5}$$

where we have used the assumption that the threshold distribution is uniform in the vicinity of $\langle u_c \rangle$ in relating p_c to u_c. From Figure 4 we can see that the stiff system scales as $L^{-2/3}$, while the soft systems deviates. We conclude that we cannot detect spatial correlation in the failure process beyond an uncorrelated percolation process for $e = e_{\text{stiff}}$.

We now proceed to study the onset of localization. Figure 5 shows the critical load σ_c as a function of e for systems of size $L = 32$ to $L = 256$. As e decreases, we observe that σ_c drops from the ELS fiber bundle value, goes through a crossover and ends in a stable σ_c for each L in the soft regime. We define e^* by setting

$$\sigma_c(e^*) = \tfrac{1}{2}[\sigma_c(e_{\text{stiff}}) + \sigma_c(e_{\text{soft}})]. \tag{6}$$

We then define

$$\sigma_c^*(e) = \sigma_c(e) - \frac{\alpha_{\sigma_c}}{\log_{10}[N]}. \tag{7}$$

We show $\sigma_c^*(e)$ *vs.* $\log_{10}[e/e^*]$ in the insert in Figure 5. As the correction term $-\alpha_{\sigma_c}/\log_{10}[N] \to 0$ in the macroscopic

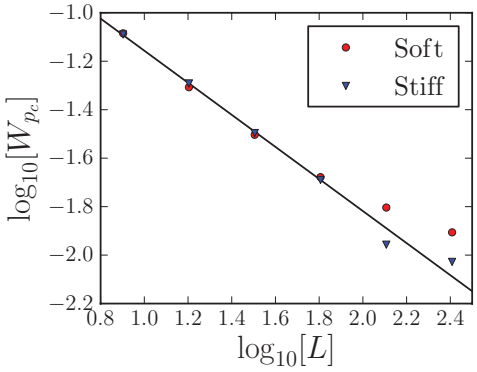

FIG. 4. (Color online) Fluctuations of p_c, $W_c = \sqrt{\langle p_c^2\rangle - \langle p_c\rangle^2}$ plotted against L for $L = 8$ to $L = 256$. The slope of the black line is $-2/3$. The stiff system follows the slope, while the soft systems deviates.

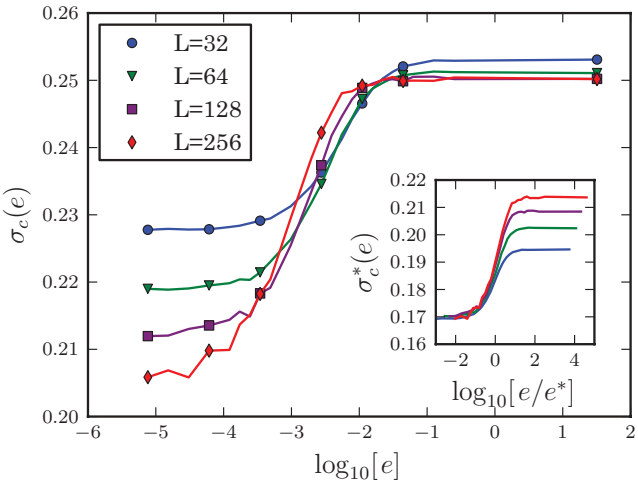

FIG. 5. (Color online) Critical load σ_c plotted against $\log_{10}[e]$ for several system sizes. The insert shows the rescaled σ_c^* plotted against $\log_{10}[e/e^*]$, demonstrating data collapse.

limit, we know that the curve never grows past $\sigma_c(e^*) = 0.25$. The largest gradient in $\sigma_c(e)$ seem to converge around

$$\frac{\Delta\sigma_c(e)}{\Delta \log_{10}[e/e^*]} = 0.03, \tag{8}$$

and the shape of the curve is kept. The onset of localization is *not* a phase transition, but a *crossover:* there are no divergences anywhere in the derivative of this curve.

The following picture then emerges: For a given elastic constant e, the breakdown process starts out as described by the ELS fiber bundle model. The spatial correlation between the failing fibers seems to be so weak that it can be described as an uncorrelated percolation process. If the elastic constant e is large enough, the system will undergo both the ELS fiber bundle model failure point and the percolation transition. Depending on the threshold distribution, the ordering of the two events, the ELS failure point and the percolation transition, may be reversed. With lower elastic constant, localization sets in and breaks off the ELS fiber bundle breakdown process. When localization sets in, all failure activity is then essentially limited to the rim of a growing cluster of failed fibers.

Our two main findings are as follows: (1) The onset of localization is an instability, not a phase transition; this is in contrast to conclusions drawn in earlier literature on fracture [4,5]. (2) A finite fraction of fibers must fail for localization to set in; this is also different from earlier claims in the literature [14,15].

We thank M. Grøva, S. Pradhan, S. Sinha, and B. Skjetne for useful discussions. This work was partially supported by the Norwegian Research Council through Grant No. 177591. We thank NOTUR for allocation of computer time.

[1] J. Schmittbuhl, S. Roux, J. P. Vilotte, and K. J. Måløy, Phys. Rev. Lett. **74**, 1787 (1995).
[2] J. Schmittbuhl and K. J. Måløy, Phys. Rev. Lett. **78**, 3888 (1997).
[3] D. Bonamy and E. Bouchaud, Phys. Rep. **498**, 1 (2011).
[4] S. Zapperi, P. Ray, H. E. Stanley, and A. Vespignani, Phys. Rev. Lett. **78**, 1408 (1997).
[5] A. Garcimartin, A. Guarino, L. Bellon, and S. Ciliberto, Phys. Rev. Lett. **79**, 3202 (1997).
[6] N. Yoshioka, F. Kun, and N. Ito, Phys. Rev. E **82**, 055102(R) (2010).
[7] S. Pradhan, A. Hansen, and B. K. Chakrabarti, Rev. Mod. Phys. **82**, 499 (2010).
[8] G. G. Batrouni, A. Hansen, and J. Schmittbuhl, Phys. Rev. E **65**, 036126 (2002).
[9] A. E. H. Love, Philos. Trans. R. Soc. A **228**, 377 (1929).
[10] K. L. Johnson, *Contact Mechanics* (Cambridge University, Cambridge, England, 1985).
[11] L. D. Landau, L. P. Pitaevskii, E. M. Lifshitz, and A. M. Kosevich, *Theory of Elasticity*, 3rd ed. (Clarendon, Oxford, 1986).
[12] F. T. Peirce, J. Text. Ind. **17**, 355 (1926).
[13] H. E. Daniels, Proc. R. Soc. London A **183**, 405 (1945).
[14] D. G. Harlow and S. L. Phoenix, Int. J. Fract. **17**, 601 (1981).
[15] R. C. Hidalgo, Y. Moreno, F. Kun, and H. J. Herrmann, Phys. Rev. E **65**, 046148 (2002).
[16] S. D. Zhang and E. J. Ding, J. Phys. A **28**, 4323 (1995).
[17] M. Kloster, A. Hansen, and P. C. Hemmer, Phys. Rev. E **56**, 2615 (1997).
[18] D. Stauffer and A. Aharony, *Introduction to Percolation Theory* (Taylor and Francis, London, 1994).
[19] X. Feng, Y. Deng, and H. W. J. Blöte, Phys. Rev. E **78**, 031136 (2008).
[20] J. Schmittbuhl, A. Hansen, and G. G. Batrouni, Phys. Rev. Lett. **90**, 045505 (2003).
[21] H. E. Daniels and T. H. R. Skyrme, Adv. Appl. Probab. **21**, 315 (1989).

Making the case of GPUs in courses on computational physics

Submitted to European Journal of Physics

Paper III

Is not included due to copyright

Universality classes in constrained crack growth

Submitted to Physics Review Letters

Paper IV

Is not included due to copyright

Local dynamics of a randomly pinned crack front: A numerical study

In preparation

Paper V

On the universality classes found in interfacial brittle fracture

In preparation

Notes:

This paper is in preparation, awaiting improved statistics. Unfortunately, this requires quite large systems ($L \leq 256$), and parts of the analysis are relatively time consuming, so this data was not available in time for the deadline for this thesis. In my opinion, the current data show the trends predicted by the theory derived within, but better statistics are needed to conclude with more certainty. The contents complete the picture on in-plane fracture obtained using our model so far.

Paper VI

Is not included due to copyright

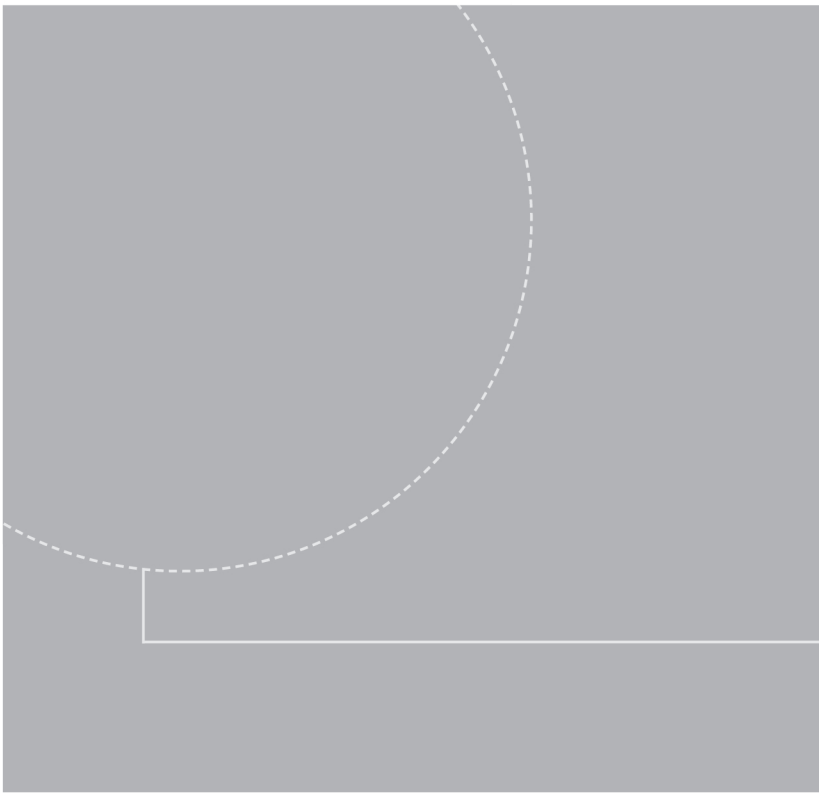

ISBN 978-82-471-4261-5 (printed version)
ISBN 978-82-471-4262-2 (electronic version)
ISSN 1503-8181

NTNU – Trondheim
Norwegian University of
Science and Technology